International
Progress Report

IPR-04-40

Äspö Hard Rock Laboratory

Äspö Task Force

Modellnig of Task 6A and 6B

Daniel Billaux

ITASCA Consultants S.A.

June 2003

Svensk Kärnbränslehantering AB
Swedish Nuclear Fuel
and Waste Management Co
Box 5864
SE-102 40 Stockholm Sweden
Tel 08-459 84 00
+46 8 459 84 00
Fax 08-661 57 19
+46 8 661 57 19

Äspö Hard Rock
Laboratory

Report no.
IPR-04-40
No.
F65K
Author
Daniel Billaux
Date
June 2003
Checked by
Date

Approved
Christer Svemar
Date
2005-01-12

Äspö Hard Rock Laboratory

Äspö Task Force

Modellnig of Task 6A and 6B

Daniel Billaux

ITASCA Consultants S.A.

June 2003

Keywords: Modelling, Tracer, Transport, Fracture, Site characterisation, Performance assessment

ANDRA

NATURE DU DOCUMENT : *NATURE OF DOCUMENT*: RAPPORT	Identification / *Identification*: G RP 0ITA 03.001

Émetteur *Originator*: DIRECTION SCIENTIFIQUE Service Milieux Géologique	Repère support/Secrétaire : *Support ref./Secretary:* GRP0ITA001doc	Date d'origine : *Original date*: 19/06/2003	Page *Page*: 1/59

ÄSPÖ MODELLING TASK FORCE

TASK 6A AND 6B MODELLING

Documents associés / *Associated documents*:

Titulaire / *Supplier*: **ITASCA Consultants, S.A.**	N° du marché : *ANDRA contract or order number:* 021821AVE	
	Référence du titulaire : *Supplier's identification:* Itasca	Visa ANDRA pour diffusion *OK Andra for distribution* Nom / *Name* : H. Benabderrahmane Visa / *Signature*:

Ind. *Ind.*:	Date : *Date:*	Nom et visa Rédacteur : *Written by (1):*	Nom et visa Vérificateur : *Reviewed by(1):*	Nom et visa Approbateur : *Approved by (1):*
B	19/06/03	Daniel Billaux	Benoit Paris	Benoit Paris

(1) : Name and signature.

ANDRA

RÉVISIONS / *REVISIONS*

Révisions / *Revisions*		Modifications / *Modifications*
Ind. / *Ind.*	Date / *Date*	
A	13/02/2003	Emission initiale
B	19/06/2003	Prise en compte des remarques et des commentaires ANDRA

ANDRA

Données documentaires pour le fonds de référence

Code(s) WBS :

-

- D2SEPAE25

-

Mots clés :

- Projets	:	Profond
- Système	:	Milieu Géologique
- Localisation	:	Suède
- Sous-localisation	:	Laboratoire souterrain d'Äspö
- Discipline scientifique	:	Modélisation hydrogéologique
- Type études	:	
- Matériaux/Milieu	:	Milieu cristallin fracturé
- Sous-milieu / matière	:	
- Termes techniques	:	Ecoulement, transport, traceur, fracture, caractérisation, performance

Prestataire(s) concerné(s) :

-

Positionnement dans l'arborescence documentaire du projet :

-

Fichier(s) informatique(s) :

Oui ☐ *Non* ☐

Résumé :

Oui ☐ *Non* ☐

Sammanfattning

Task 6 i ”Äspö Task Force on Modelling of Groundwater Flow and Transport of Solutes” har som mål att förbättra övergången från platsbeskrivning till säkerhetsanalys när det gäller transport av lösta ämnen i sprucket berg. De första delarna (6A och 6B/B2) är inriktade på platsen för TRUE-1 ”Feature A”och på skalan fem meter.

Task 6A består av att modellera spårämnesförsök STT-1b som genomförts inom TRUE-1 programmet. Vi betraktar här ”Feature A” som plan. Ett nätverk av dominerande flödeskanaler representerar strömningsfältet. De delar av porutrymmet där ingen strömning förekommer representeras av ”icke-strömmande element” av sprickfyllnadsmineral, mylonit och diorit. Ett spårämne kan tränga in i dessa element där det sedan rör sig normalt från sprickan genom diffusion. Vi arbetar inom ramen för advektions-dispersions-diffusionsmodellen (ADD). Dvs de processer som bidrar till att forma genombrottskurvan är advektion, axiell dispersion, blandning där flödeskanaler möts, adsorption på kanalväggarna, diffusion in i de delar av porutrymmet där ingen strömning sker och adsorption i porerna i denna del av porutrymmet.

Kalibreringen av modellen startar med nätverkets geometri och övergår sedan till att hantera fördelningen av kanalernas konduktivitet. Nätverket görs något anisotropt med kanallängder och –frekvenser som anpassas så att det genomsnittliga endimensionella avståndet mellan korsningar mellan kanaler hamnar nära den indikerade korrelationslängden. En högkonduktiv zon läggs in mellan KXTT2 och KXTT3 för att efterlikna den tryckhöjdsrespons som fås i dessa båda mätpunkter.

Därefter används genombrottskurvor för spårämnen för att kalibrera flödes/hastighetssambandet genom att välja konduktivitets/sprickviddssamband. Dispersionskoefficienten och matrisens diffusionsegenskaper väljs sedan genom att först ansätta i förväg givna värden och sedan modifiera dessa för att förbättra anpassningen mellan beräknade och mätta genombrottskurvor. K_d och K_a väljs sedan för olika material och spårämnen varvid ambitionen är att ligga så nära de i förväg specificerade värdena som möjligt.

Task B och B2 utgör anpassningen av spårämnesförsöket STT-1b till en tidsskala som är relevant för säkerhetsanalyser genom att anpassa randvillkoren så att den hydrauliska gradienten mellan injektions- och provtagningspunkten blir i storleksordningen 0,1 %. Task 6B hanterar bytet av tidsskala helt enkelt genom reduktion av flödeshastigheten medan Task 6B2 också tar hänsyn till förändring av flödesmönster och trajektorier som uppträder när man lägger på en mer uniform gradient över nätverket och dessutom har en mycket större källterm för spårämnena.

Det nätverk som används i Task 6A utgör grunden för modellerna som används i Task 6B och 6B2. Efter att ha beräknat det flöde som uppstår på grund av randvillkorsförändringen förenklar vi systemet genom att ta bort alla kanaler som inte återfinns nedströms från injektionspunkten eller –linjen samt kanaler uppströms provtagningspunkten eller –linjen.

Även om de resultat som vi får inte visar något oförväntat beteende kan vi inte anse att det vara visat att användning av ADD-modellen är tillräckligt för det betraktade problemet (dvs uppskattning av egenskaper på en tidsskala och extrapolation till en mycket längre tidsskala). För det första var vi tvungna att, för att kunna kalibrera modellen mot genombrottskurvor i försökets tidsskala, anta att modellens strömningsfält är något annorlunda än det som beskrivs av provtagningen i försöket med avseende på jod och strontium (4/59 Report G RP 0 ITA 03-003/B juni 2003). Detta antyder att vi kan förbise något av de fysikaliska förlopp som pågår. För det andra ger två kurvanpassningar för strontium med respektive utan matrisdiffusion extrema skillnader i förutsägelserna för Task 6B och 6B2. Jämfört med dessa stora osäkerheter och med en given uppsättning statistiska egenskaper för sprickan är variabiliteten i prognostiserad respons från realisering till realisering liten. Dessutom förefaller en känslighetsanalys en större variabilitet i responsen i 6B (randvillkoret ”focused flow”) än i 6B2 (randvillkoret ”generalised flow”).

ABSTRACT

Task 6 of the "ÄSPÖ Task Force on Modeling of Groundwater Flow and Transport of Solutes" aims at improving the transition from site characterization to performance assessment for solute transport in fractured rock. The first parts (6A and 6B/B2) focus on the TRUE-1 site "Feature A", at a five meters scale.

Task 6A consists of modeling tracer test STT-1b, performed within the TRUE-1 program. We consider Feature A as planar. A network of preferential flow channels represents the flow field. The immobile pore space is represented by gouge, mylonite and diorite "non flowing" elements. These elements may be invaded by the tracer, which then moves in them by diffusion only, normal to the channels. We work within the framework of the Advection-Dispersion-Diffusion (ADD) model: the processes contributing to the shape of breakthroughs are: advection, longitudinal dispersion, mixing at intersection, adsorption on channel sides, diffusion into the immobile pore space, and adsorption in the pores of the immobile pore space.

Calibration of the model starts with the geometry of the network, and then deals with the channels conductivity distribution. The network is made slightly anisotropic, with channel lengths and density such that the average 1D length between intersections is close to the indicated correlation length. A highly conductive zone is introduced between KXTT2 and KXTT3 in order to simulate the hydraulic head responses of these two wells.

Non-sorbing tracer breakthrough is then used to calibrate the flow/velocity relationship through the choice of a conductivity/aperture law. Coefficient of dispersivity and matrix diffusive properties are then chosen, by using first the values given in the specifications, and modifying them to improve breakthrough calibration. The final stage of the calibration process concerns sorbing tracer breakthrough curves. Kd's and Ka's are chosen for the various materials and tracers, trying to keep numbers as close to the specified values as possible.

Tasks B and B2 are the adaptation of the STT-1b test to Performance Assessment time scale, modifying the boundary conditions to obtain a gradient between the injection and the extraction wells in the order of 0.1%. While B simply deals with the time scale by reducing flowrates, B2 also looks at the change in flow pattern and trajectories, imposing a more uniform gradient through the network, and using a much larger source for the tracers.

The network used for Task 6A is the basis of the Task 6B and 6B2 models. After computing flow due to the changed boundary conditions, we simplify the system by removing all channels which are not located downstream of the injection well or injection line, and upstream of the recovery well or recovery line.

Although the results we obtain show no unexpected behaviour, we cannot consider that the use of the Advection-Dispersion-Diffusion model (or ADD model) has been proved sufficient for the problem at hand (i.e. estimation of properties at one time scale, then extrapolation to a much larger time scale). First, at test time scale, in order to calibrate the model to Co breackthrough, we had to assume it samples a flow field that is

somewhat different from the flow field sampled by Iodine and Strontium. This shows we may overlook some of the physics involved. Second, two fits for Strontium with and without matrix diffusion yield extreme differences in the predictions for Tasks 6B and 6B2.

Compared to these large uncertainties, given a set of statistical properties for the fracture, the variability in its predicted response from realisation to realisation is quite small. Also, a sensitivity study seems to point out to a larger variability of the response with the 6B ”focussed flow” boundary conditions than with the 6B2 ”generalized flow” boundary conditions.

CONTENTS

LIST OF TABLES

LIST OF FIGURES

1 INTRODUCTION

This document is the final report for the participation of the ANDRA/ITASCA team to parts A and B of the Task 6 of the ÄSPÖ Task Force on Modeling of Groundwater Flow and Transport of Solutes.

The general aims of Task 6 are described in Benabderrahmane et al (2000). Task 6 seeks to provide a bridge between site characterization (SC) and performance assessment (PA) approaches to solute transport in fractured rock. There is no strict formalism to distinguish between SC-type and PA-type models. However, it is generally accepted that PA models are simpler and physically less realistic than SC models. Task 6 tries to bridge the gap between both types of models by applying the two approaches for the same tracer experiment, and also for PA boundary conditions.

The objectives of Task 6, as stated in the above reference, are to:

1. Assess simplifications used in PA models.
2. Assess the constraining power of tracer (and flow) experiments for PA models.
3. Provide input for site characterization programs from a PA perspective (i.e., provide support for site characterization program design and execution aimed at delivering needed data for PA).
4. Understand the site-specific flow and transport behavior at different scales using SC models.

Task 6 focuses on the 50 to 100 meter scale, which is frequently the critical scale for geosphere retention. However, in order to allow for a more direct comparison, initial simulations are carried out on the TRUE-1 site at the 5-meter scale. Therefore, the Task includes studies at two scales:

- Single fracture scale, based on the TRUE-1 site. The purpose of the modeling study is to assess how different conceptualizations of a single fracture (Feature A) compare to each other.
- Fracture network (block) scale: a synthetic block based mostly on the TRUE Block Scale volume has been constructed by SKB and will be used by all modeling groups. The main purpose is to assess how uncertainties are carried and reinforced from the Site Characterization time scale to the Performance Assessment time scale.

Flow and transport at the two spatial scales identified above are addressed by applying both SC-type models and/or PA-type models to two different transport modes characterized by different temporal scales:

- Tracer test time scale (Tracer test mode): The selected sets of TRUE-1 tracer experiments are modeled. The purpose of the modeling study is to provide constraints to all the models before invoking assumptions for PA time scale predictions.

- PA time scale (PA mode): Nuclide or sorbing tracer transport modeling with PA type boundary conditions is performed. Modelers must honor the material properties used for the "tracer test time scale" transport modeling.

Flow and transport at the two spatial scales are thus analyzed for both current boundary conditions and for PA-relevant time scales; i.e., four different combinations of spatial and temporal scales are addressed.

The four different combinations mentioned above structure the organization of Task 6 into separate sub-tasks. To these four sub-tasks is added an intermediate one, consisting of the construction of the synthetic model for network scale. Task 6 therefore consists of 5 sub tasks, with the first two parts (6A and 6B) focusing on the TRUE-1 site at a 5 meters scale (more precisely, the water-conductive fracture named Feature A), the third part (6C) being the building of the network scale model, and the last two parts (6D and 6E) focusing on the network scale modeling. In each pair of sub-tasks at a given spatial scale (i.e. 6A/6B or 6D/6E), the first sub-task deals with "experimental" time scales (i.e. from days to years), while the second one deals with "Performance Assessment" time scales (i.e. centuries to 10^6 years).

Task 6A consists of modeling tracer test STT-1b, performed within the TRUE-1 program, and already modeled by the members of the previous Task 4E. Objectives for Task 6B are to run simulations based on Task 6A model with boundary conditions and time scales relevant for performance assessment calculations. This implies adapting the transport and retention processes modeling, such as simplifying the transport pathways or testing the effects of diffusion and retention into the matrix.

ITASCA Consultants did not participate in the Task 4E exercise. Our first objective was therefore to improve our knowledge of Feature A by performing the Task 6A, that is reproducing the experimental breakthrough curves of the STT-1b tracer tests for several non-reactive and reactive species. All simulations are performed with the ITASCA code *3FLO* (Billaux and Paris, 2001).

2 Modelling Tasks

The modeling task specifications are described in Selroos and Elert (2001), and in Elert and Selroos (2001).

2.1 Task 6A

Task 6A consists of modeling tracer test STT-1b, performed within the TRUE-1 program, and previously modeled by the members of Task 4E. It is a kind of "rehearsal" task, so that teams who have not yet modeled "Feature A" can build realistic simulations based on the experimental data provided.

The geometry of the test, using a radially converging flow, is detailed in section 3.1. It is aimed at testing a single structure, named "Feature A".

2.2 Task 6B

Task B aims to adapt the Task A modeling for Performance Assessment conditions and time scales and to study the influence of the assumptions made.

The objective of this part of the work is the adaptation of the STT-1b test to Performance Assessment conditions through the following assumptions:

- The observed flow field is modified in such a way that the pressure gradient between the injection and the extraction wells is in the order of 0.1%;
- The background flow field is modified in order to account for the absence of the tunnel impact and therefore prescribe a hydraulic gradient oriented from KXTT1 towards KXTT3.

The same flow paths and material properties are assumed for Task 6B as in Task 6A. Therefore, the geometry of the 6B model is exactly the same as the geometry of the 6A model. Note that because the flow conditions are radially converging, the flow paths visited by the tracers are likely to be quite narrow.

2.3 Task 6B2

Task 6B2 has the same aim and time scale as task 6B, but considers other boundary conditions: whereas the task 6B boundary conditions simply reduced the flowrates from task 6A, task 6B2 boundary conditions use a large source dimension and no radial pumping, in order to mimic more closely "Performance Assessment" conditions, as shown in Figure 2-1 taken from Elert and Selroos (2001). More precisely: it is assumed that the flow regime in Feature A is governed by its intersection with two fractures (X and Y) positionned at a distance of 15 m from each other, and roughly parallel. The specified boundary conditions are reproduced in Figure 2-2. As can be seen from these figures, the resulting tracer paths are likely to be more distributed than the radially converging flow paths used for Task 6B.

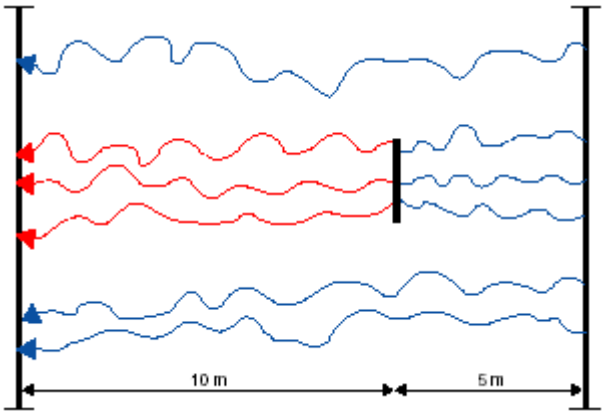

Figure 2-1 Principle of Task 6B2 geometry (Elert and Selroos, 2001)

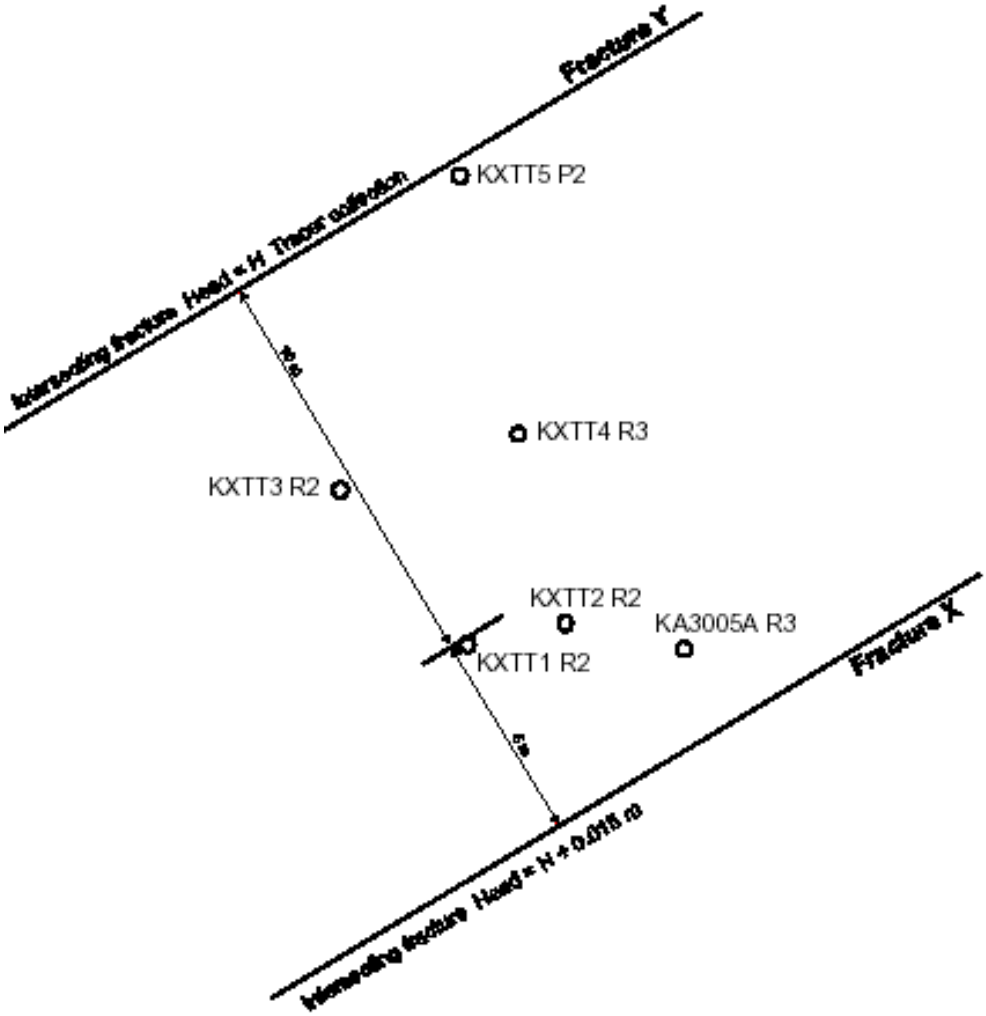

Figure 2-2 Task 6B2 boundary conditions (Elert and Selroos, 2001)

3 Model description

3.1 Geometrical description

The geometry of our model is based on geological and hydrogeological information. We briefly review these data before describing the model.

3.1.1 Brief description of the geological medium (Feature A)

The following information and figure are taken from Winberg *et al.* (2000).

Feature A is believed to follow a fault plane included in a zone of reactivated mylonite and bounded by a rim zone consisting of altered Äspö diorite forming a band of disturbed rock (Figure 3-1). The fracture extent is estimated at 10-20 m, for a total thickness varying between 0.05 and 0.09 m. The fracture physical aperture is assumed to be in the range of 0.001 to 0.003 m. The fault plane is not centered on the mylonite along its extent and water could also be in contact with Äspö diorite.

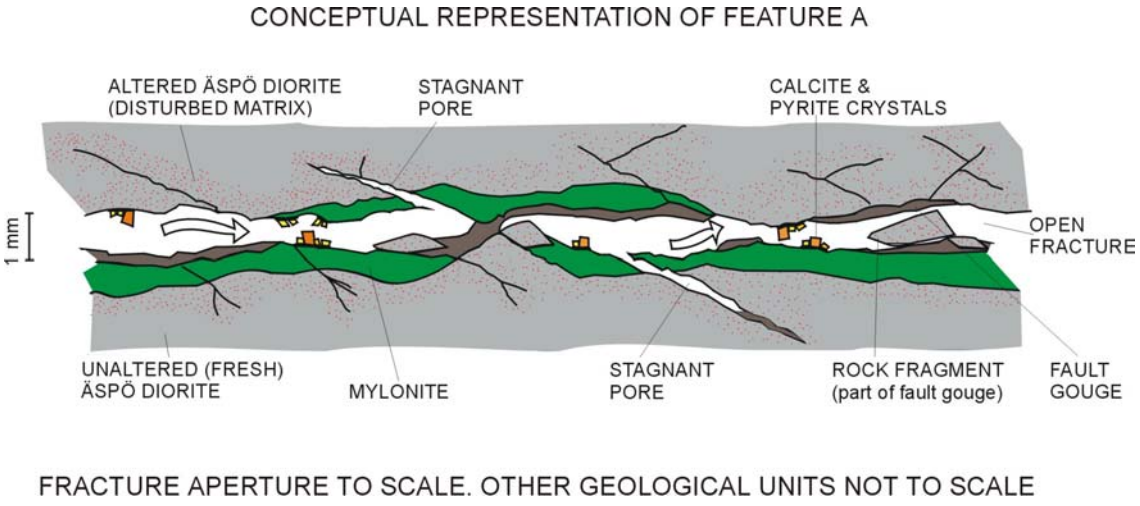

Figure 3-1 Schematic conceptual representation of Feature A in cross section (not to scale)

The main fracture minerals are calcite, fluorite, quartz, K-feldspar and pyrite. There is evidence of clay minerals as an outer rim of the fracture mineral coating which suggests that gouge material might be present in Feature A.

3.1.2 Hydrogeological information

Measurements have been made in the five boreholes intercepting Feature A. These intercepts form a planar structure with a fitted orientation of N29W/79E (Figure 3-2).

The interval depths are given in Table 3-1 and the steady-state head measurements are indicated in Table 3-2.

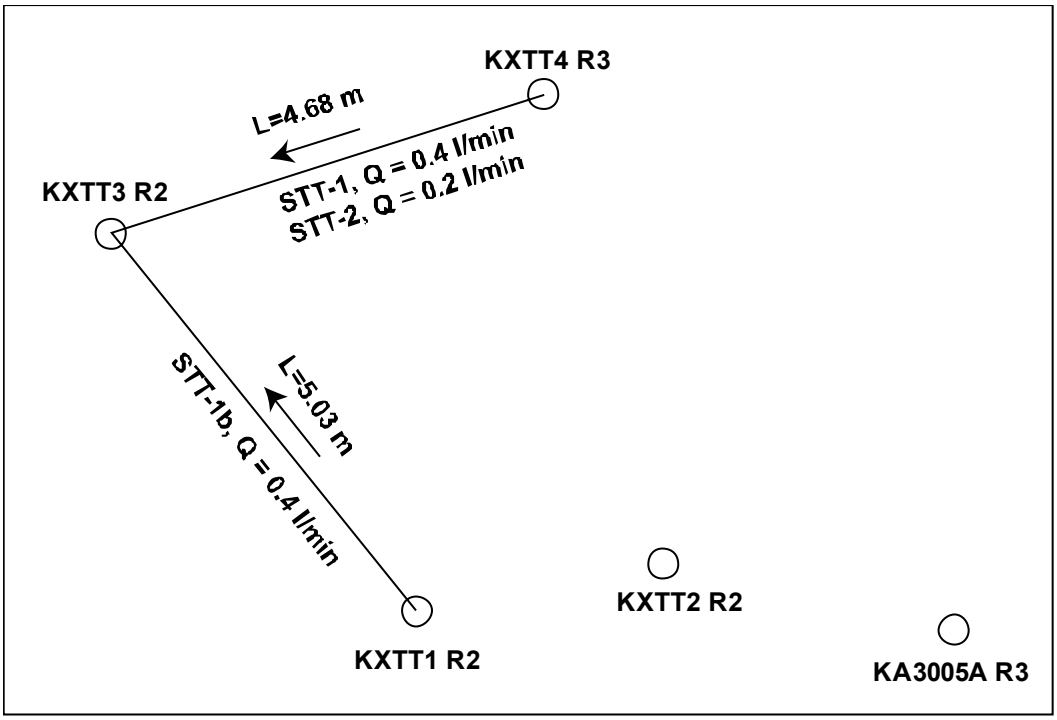

Figure 3-2 Test geometry, pumping flow rates (Q) and borehole intersection pattern with Feature A for the tracer tests STT-1, STT-1b and STT-2

Although the natural hydraulic gradient is directed from KXTT3 towards KA3005A, *i.e.* in the direction of the tunnel, there is no available information supporting the assumption that Feature A would be in hydraulic contact with the tunnel. Cross-holes interference testing showed that Feature A is well isolated even though the site investigations proved that it is connected to zone NW-2' and to Feature B.

Hydraulic site characterization data (Winberg *et al.*, 2000) gave values of transmissivity in the (large) range of 8.10^{-9} to 1.10^{-6} m^2/s, with the most permeable formation in the vicinity of KXTT3. Interpretations of the well tests emphasized a flow dimension number almost always higher than 2, which might be an indication of the existence of highly permeable pathways in the modeled system, or of flow paths outside the fracture plane.

Borehole	Interval	Length	Easting	Northing	Z	Strike	Dip
KXTT1	R2	15.79	2323.26	7435.27	-403.41	319	79
KXTT2	R2	15.04	2323.80	7432.78	-402.95	344	74
KXTT3	R2	14.10	2321.41	7438.02	-399.54	325	78
KXTT4	R3	12.10	2322.29	7433.66	-398.28	326	76
KA3005A	R3	44.97	2324.72	7430.02	-403.43	340	88

Table 3-1 Borehole – Feature A intercepts coordinates (in local reference system)

The estimated specific storage is in the range 1.10^{-6} to 2.10^{-5} m^{-1}.

There is not a lot of information regarding the correlation length. Winberg (1996) assumed a correlation length in a range of 0.3 to 0.4 m, based upon the dispersivity estimated from the preliminary tracer tests.

Borehole section	Hydraulic head (masl)
KXTT1 R2	-53.02
KXTT2 R2	-53.03
KXTT3 R2	-52.62
KXTT4 R3	-52.88
KA3005A R3	-53.57

Table 3-2: hydraulic head in borehole sections prior to the STT-1b test

The STT-1b tracer test was performed using a radially converging flow geometry, with pumping in borehole section KXTT3 R2 and injection of tracer in borehole section KXTT1 R2, both penetrating Feature A (Anderson et al, 1999). The travel distance between the boreholes is 5.03 meters.

The evolution of head with time, due to the long term pumping that preceded the STT-1b tracer injections, is displayed on Figure 3-3 (values are taken from Task 6 Data Delivery n°1). Note that the pumping flow rate has been set high enough to reverse the natural hydraulic gradient.

Comparing these results with the well bore locations mapped on Figure 3-2, one can notice the singular behavior of KXTT2, whose response seems to be much more influenced by pumping than would be expected when comparing to KXTT1. This observation suggests the existence of preferential pathways between KXTT2 and the

pumping well KXTT3, which must be taken into account in our conceptual model. This observation is consistent with the flow dimension greater than 2, as discussed above. We therefore introduce a highly conductive zone between KXTT2 and KXTT3.

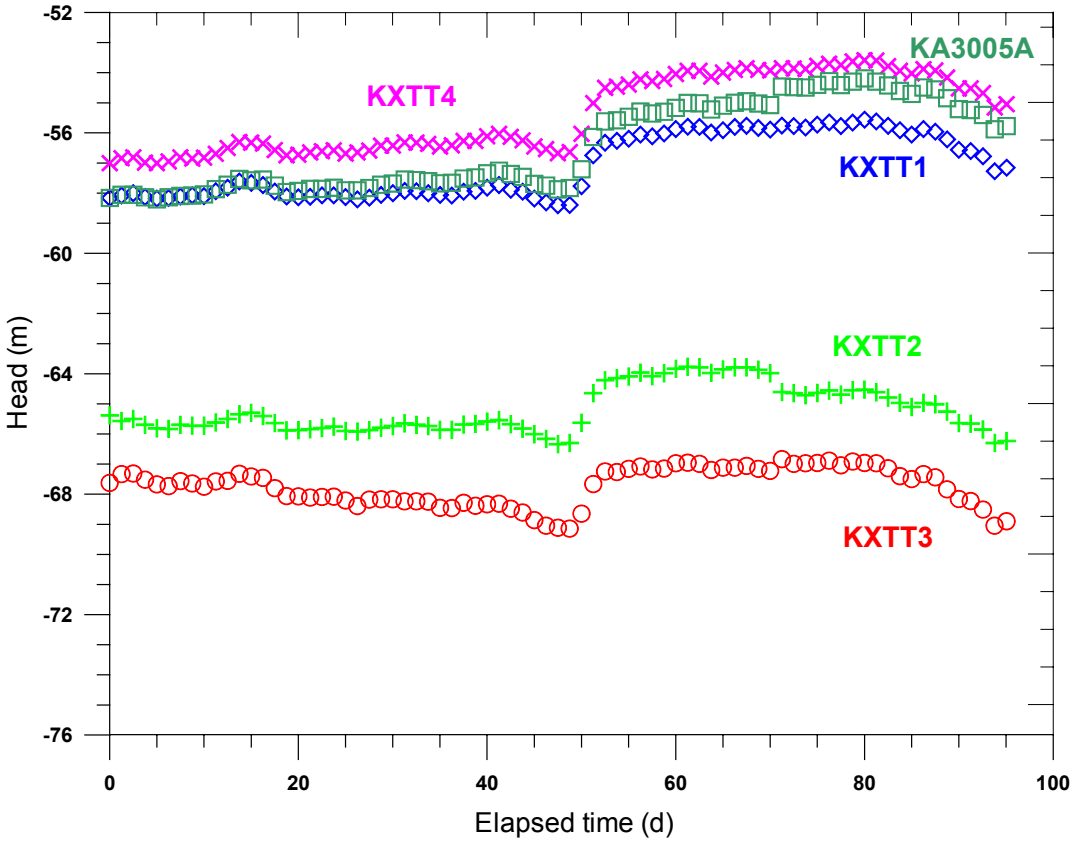

Figure 3-3 Measured hydraulic heads due to long term pumping

3.1.3 Conceptual model

Our conceptual model is based on the described geometry and on the hydraulic head measured at the five boreholes during the long term pumping prior to the tracer injection.

Based on the system geometry, we adopted a 2-D approach, *i.e.* considering Feature A as a planar structure, with a model extension of 20 × 20 m. As explained above, a highly conductive zone has been introduced between KXTT2 and KXTT3. The advective pore space is considered as a network of preferential flow channels, with a distribution of properties, connected with each other.

In-plane aperture is heterogeneous in several senses: first, channelling in itself is a representation of preferential flow paths, i.e. of a heterogeneous plane. Second, the properties of the individual flow channels such as orientation, length, and conductivity/aperture are taken from statistical distributions. Note that because of complete mixing at channel intersections, this forces a strong heterogeneity of the tracer paths: even in a focused test such as 6A/6B (i.e. radially converging flow field), the tracer will follow not one but several paths. Third, based on the analysis of heads during the pumping test, we impose a "high transmissivity zone" between KXTT2 and KXTT3.

Since the orientation distribution of the channels in the fracture plane is anisotropic, our transmissivity field is too. We are not explicitly introducing a correlation length in our model. However, we chose the channel network density and length distribution so that the average distance between intersections is equal to the correlation length indicated in the specifications.

Besides the "free-flowing fracture space" (i.e. fracture space, in which flow is computed from boundary conditions, in which advection is allowed and porosity is assumed to be 100%), the immobile pore space is represented by gouge, mylonite and diorite elements, which may be invaded by the tracer which then moves in these elements by diffusion only. Note that diorite is present everywhere next to flow channels, but may be separated from them by some thickness of gouge or mylonite, as shown in Figure 3-4. Note that this conceptual representation, although it leads to a fairly complex model, is a simplification of the detailed conceptual model as illustrated by Figure 3-1. The rationale for choosing this representation is to try to represent the various aspects of the immobile pore space with the smallest number of components: "diorite" represent the "relatively low porosity, but large volume" material that is likely to have a small effect for short term but be dominating the long term response. Then "gouge" and "mylonite" are taken as two contrasted fracture fillings/coatings, with one quite porous and the other closer to the diorite values.

Note that the model automatically generates one category of immobile pore space: stagnant zones exist where pipes end up as "dead-ends". Such pipes cannot be invaded by advection (no flow entering them), but tracer particles may reach them by diffusion. Even when the model is simplified (as discussed in section 3.6), we keep such "dead-end pipes" in order to represent diffusion into stagnant zones.

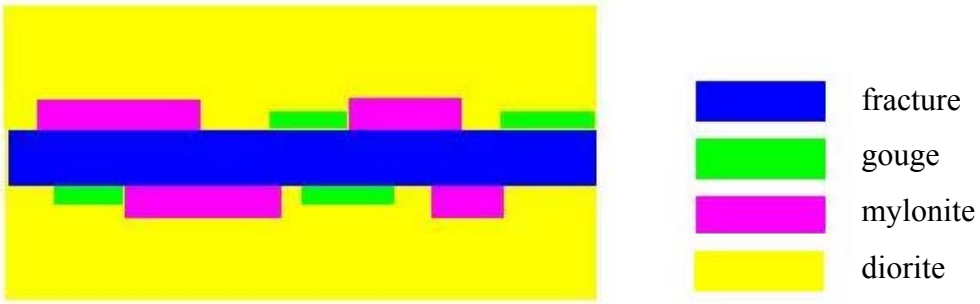

Figure 3-4 Pore space conceptual model

3.2 Processes considered

The processes we are considering are the following:

- Advection.
- Dispersion, represented numerically by two "sub-processes":
  - Application of a longitudinal dispersivity within the flow paths;
  - Complete mixing at channel intersections.
- Adsorption onto the fracture sides.

- Diffusion into immobile pore space: matrix, gouge.
- Adsorption into the pores of the immobile pore spaces.

3.3 Numerical model

3.3.1 Flow

For this project, we use the ”network flow” module of the *3FLO* code (Billaux and Paris, 2001), in steady-state mode. In this 3D model, the flow field is restricted to a network of connected one-dimensionnal channels. The steady state flow equation in each pipe is therefore very simple:

$$T \frac{\partial^2 h}{\partial x^2} = 0 ,$$

where: T is the integrated hydraulic transmissivity of each pipe, h is the hydraulic head, and x is the coordinate along the pipe.

This is solved by the Galerkine finite element method, with any channel end or channel intersection being a node, and a finite element (or “pipe”) being the portion of a channel between two nodes. This yields heads at all nodes and flowrates in all pipes. Note that here we further restrict the channels in one given plane, so we end up with a two-dimensional model made of interconnected 1D pipes. The pipe lengths range from 0.01 m (arbitrary minimum length: nodes connected by shorter pipes are merged) to 3.8 m, with an average at 0.4 m (as discussed elsewhere). The flow solution shows a relative precision (ratio of unbalanced algebraic flowrates at nodes to actual flowrates in pipes) of the order of 10^{-5}.

3.3.2 Transport

The *3FLO* transport module uses the Discrete Parcel Random Walk approach.

In this method, source terms are modelled by introducing a large number of particles, each particle holding a relevant mass (or number of moles) of one or more components. In other words, for any chemical component, the sum of the various mass (moles) attached to the whole set of particles present in a given block (pipe) represent the soluble concentration.

Each particle moves in the block (pipe) network with the flow velocity (convective transport), its coordinates at time $t + \Delta t$ being:

$$x_i^{t+\Delta t} = x_i^t + V_j^t \Delta t ,$$

where V_j^t is the pore velocity vector in the block (pipe). An additional displacement is imposed to each particle in order to simulate hydrodynamic dispersion. This dispersive displacement is computed by randomly sampling a Gaussian distribution with zero mean and a variance depending on the time step and the dispersion coefficient. The “dispersive” displacement is added three times (one longitudinal and two transversal displacements) in 3D blocks, and only one time (longitudinal) in the 1D pipes. Note that by adding a Gaussian-distribute jump to the advective jump, we enable particles to go

upstream for part of their movement. Furthermore, complete mixing is assumed at pipe intersections, forcing the exploration or several pathways by the tracer.

The pipe dispersivity coefficient is supposed homogeneous throughout the model. Its value is adjusted during the calibration process.

The model discretization is the same for transport as for flow. The number of particles used to represent a single injection varies between 40,000 and 1,000,000. The precision for such complex runs is hard to assess. For reference, simple one-dimensional dispersive transport using 10,000 particles yields concentrations with a relative error around 5% for a Peclet number equal to 0.1.

3.3.3 Matrix diffusion

3FLO simulates "fracture to matrix diffusion" by adding virtual blocks around the pipes and allowing particles to move laterally within these blocks. At each time step, a particle contained in the pipe may enter the adjacent matrix with a given probability, depending on the time step, the pipe thickness, and the diffusion coefficient of the matrix. The probability is chosen so that the algorithm correctly simulates simple cases for which an analytical solution is known. Such a validation example is given in the appendix (chapter 7). When a particle enters into a matrix block, the displacement becomes only diffusion controlled and is assumed to remain perpendicular to the pipe axis. For each time step, the diffusive displacement is computed by randomly sampling a Gaussian distribution with zero mean and a variance depending on the time step and the diffusion coefficient.

3.3.4 Retardation

Two kinds of retardation factors are used as suggested in the modelling task specifications:

- Adsorption onto the fracture walls, described by a surface sorption coefficient (*Ka [L]*);
- Adsorption onto the bulk matrix material accessible though diffusion, described by a volume sorption coefficient ($Kd\ [L^3.M^{-1}]$).

In both cases, we simulate the retardation of the reactive species by using a simple linear relationship between the aqueous (mobile) and the solid (fixed) concentrations.

Volume retardation:

$$F_{fixed} = Kd \times C_{aqueous} \qquad (1)$$

Where:

- F_{fixed}: mass fraction in the solid phase;
- $C_{aqueous}$: aqueous phase concentration.

With F_{fixed} = mass of tracer in the solid phase / mass of solid = m_{fixed} / $(1-\omega)\ \rho_s$ (for an elementary volume)

- ω: porosity of the medium;

- ρ_s: solid density.

And $C_{aqueous}$ = mass of tracer / volume of solvent = $m_{aqueous}$ / ω (for an elementary volume)

We can therefore rewrite (1) in the following manner:

$$m_{fixed} = Kd \times m_{aqueous} \times (1-\omega)\, \rho_s / \omega$$

The total mass m_T per volume element is:

$$m_T = m_{fixed} + m_{aqueous} \qquad (2)$$

Therefore:

$$m_T = m_{aqueous} \times [\, 1 + Kd \times (1-\omega)\, \rho_s / \omega \,]$$

And:

$$m_{aqueous} = m_T / [\, 1 + Kd \times (1-\omega)\, \rho_s / \omega \,] = m_T / Rd \qquad (3)$$

Rd is known as the retardation factor.

Surface retardation:
Let us consider a fracture containing a volume of water *V* in contact with a matrix surface area *S*. The *Ka* linear relationship is:

$$F_{fixed} = Ka \times C_{aqueous} \qquad (4)$$

Where:

- F_{fixed}: mass fixed onto the fracture edges [$M.L^{-2}$] = m_{fixed} / S
- $C_{aqueous}$: aqueous phase concentration = $m_{aqueous} / V$

Combining (4) with the mass conservation equation (2) gives:

$$m_T = m_{aqueous} \times [\, 1 + Ka \times S / V \,]$$

And:

$$m_{aqueous} = m_T / [\, 1 + Ka \times S / V] = m_T / Ra\,, \qquad (5)$$

where *Ra* is an other retardation factor.

Practically, *3FLO* uses a four-step procedure for any pipe or matrix block, and for each time step:

1. Computation of the total mass (m_T) of tracer by summing the total mass held by the particles and adding the sorbed (fixed) tracer mass;
2. Computation of the new aqueous mass of tracer using equation (3) for a matrix block, or (5) for a pipe;
3. Computation and storage of the sorbed (fixed) mass of tracer;

4. Adjustment of the particle masses to reflect the new transportable mass: on each particle the initially attached mass is multiplied by the ratio of the new to the previous total soluble mass.

Note that a pipe (block) containing fixed mass and no soluble mass (i.e. no particle) will require the creation of new particles, since some part of the fixed mass will be transferred from "adsorbed" to soluble. 3FLO automatically creates the needed new particles.

3.4 Parameters

The parameters resulting from the model calibration and used for all simulations are given below in the format specified for the Task 6 Questionnaire.

Tracer	Matrix sorption coefficient Kd (m^3/kg)		Surface sorption coefficient Ka (m)		Effective matrix diffusivity De (m^2/s)	
	Task 6A	Task 6B/B2	Task 6A	Task 6B/B2	Task 6A	Task 6B/B2
I	0	0	0	0	2.00E-14	2.00E-14
Sr	1.00E-07	1.00E-07	8.00E-06	8.00E-06	1.00E-14	1.00E-14
Co	5.00E-03	5.00E-03	5.00E-02	5.00E-02	1.00E-14	1.00E-14
Tc	2.00E-01	2.00E-01	2.00E-01	2.00E-01	1.00E-14	1.00E-14
Am	5.00E-01	5.00E-01	5.00E-01	5.00E-01	1.00E-14	1.00E-14

Table 3-3 Sorption and diffusivity data for tracers in diorite, for Task 6A, 6B and 6B2.

Tracer	Matrix sorption coefficient Kd (m^3/kg)		Surface sorption coefficient Ka (m)		Effective matrix diffusivity De (m^2/s)	
	Task 6A	Task 6B/B2	Task 6A	Task 6B/B2	Task 6A	Task 6B/B2
I	0	0	0	0	2.00E-14	2.00E-14
Sr	1.00E-06	1.00E-06	8.00E-06	8.00E-06	1.00E-14	1.00E-14
Co	2.00E-03	2.00E-03	5.00E-02	5.00E-02	1.00E-14	1.00E-14
Tc	2.00E-01	2.00E-01	2.00E-01	2.00E-01	1.00E-14	1.00E-14
Am	5.00E-01	5.00E-01	5.00E-01	5.00E-01	1.00E-14	1.00E-14

Table 3-4 Sorption and diffusivity data for tracers in mylonite, for Task 6A, 6B and 6B2.

Tracer	Matrix sorption coefficient Kd (m^3/kg)		Surface sorption coefficient Ka (m)		Effective matrix diffusivity De (m^2/s)	
	Task 6A	Task 6B/B2	Task 6A	Task 6B/B2	Task 6A	Task 6B/B2
I	0	0	0	0	4.00E-12	4.00E-12
Sr	1.00E-04	1.00E-04	8.00E-06	8.00E-06	2.00E-12	2.00E-12
Co	2.00E-01	2.00E-01	5.00E-02	5.00E-02	2.00E-12	2.00E-12
Tc	2	2	2.00E-01	2.00E-01	2.00E-12	2.00E-12
Am	5	5	5.00E-01	5.00E-01	2.00E-12	2.00E-12

Table 3-5 Sorption and diffusivity data for tracers in gouge, for Task 6A, 6B and 6B2.

3.5 Model calibration and development

The parameters resulting from model calibration are the ones given in paragraph 3.4. We describe below how we chose them from the available information.

3.5.1 The STT-1b tracer test

A solution containing various tracers was injected in borehole section KXTT1 R2 as a finite pulse with duration of 4 hours. Four non-sorbing (Uranine, HTO, ^{82}Br, ^{131}I) and six weakly to moderately radioactive sorbing tracers (^{22}Na, ^{42}K, ^{85}Sr, ^{99m}Tc, ^{58}Co and ^{86}Rb) were used. After four hours of passive injection, the tracer solution was exchanged in two steps with unlabelled water. The first exchange lasted for 60 minutes and the second exchange, 100 minutes after the end of the first one, lasted for 25 minutes.

The pumping in the withdrawal section (KXTT3 R2) was 0.4 l/min.

Breakthrough curves from the STT-1b tracer test are available for HTO, ^{131}I, ^{85}Sr and ^{58}Co. ^{99m}Tc was used in the STT-1b test, but no recovery was observed. In addition the sorbing tracer, ^{241}Am is included in the modelling task, although it was not used in the STT-1b test. The purpose is to study how the retardation of more sorbing radionuclides can be extrapolated in time. However, in this case no comparison can be made with experimental data. So the model calibration is based on breakthrough curves for one non-sorbing tracer (^{131}I), for ^{85}Sr and for ^{58}Co.

The density of the water is estimated to be 1005 kg/m^3. The flow rate in the injection section was estimated to be 41.9 ml/h during the period 0 - 4 hours and 58.1 ml/h during the period 20 - 151 hours. Because of the flushing of the injection section no estimates could be made for the period 4 - 20 hours. We consider that the flow rate during the 4 - 20 hours period is the one in the first period that is 41.9 ml/h. The injection time histories of americium and technetium are assumed to be identical to that of ^{58}Co.

The concentration histories given in the Task 6 specification last a few hundred hours (I, Sr) to about 2,000 hours (Co). In fact, concentrations at the end of the histories are not zero: they are of the order of 0.1 % of the peak injection concentrations, decreasing in a regular fashion (Figure 3-5), in a way similar to a dilution experiment. There is no reason whatsoever for the concentrations dropping to zero at that time. We extend the input injection by an exponentially decreasing history, with a log-slope equal to the slope of the last decade in the input.

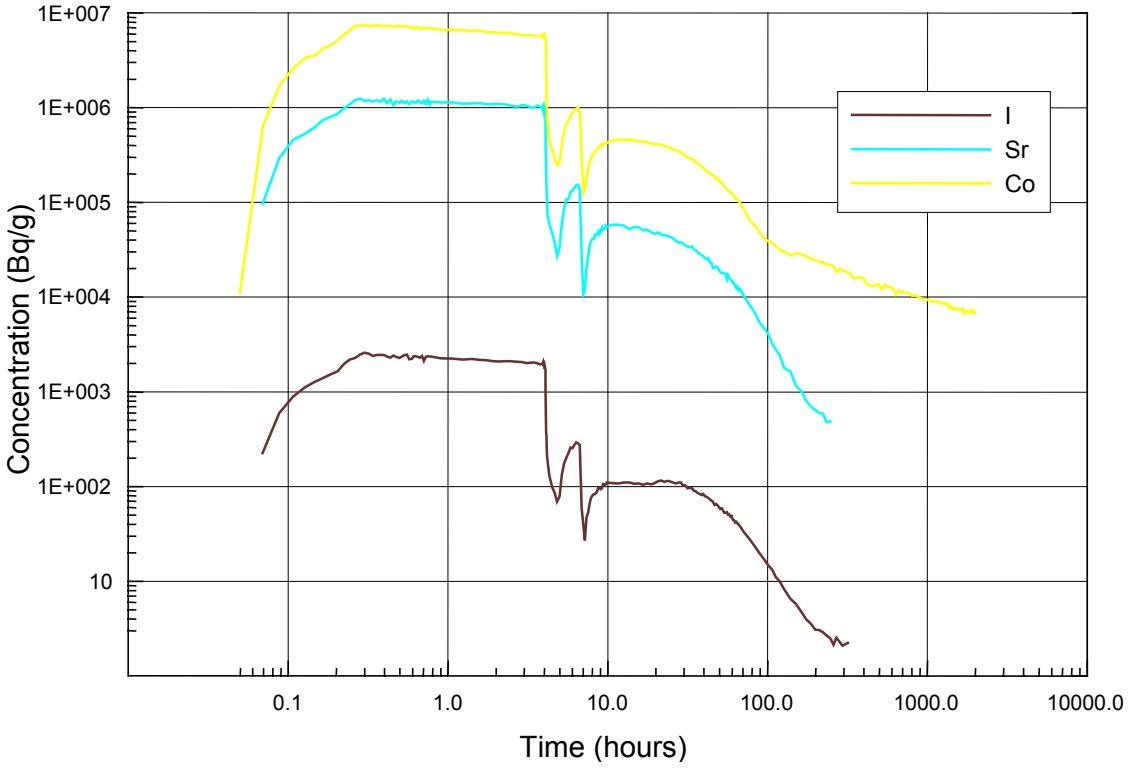

Figure 3-5 Injection concentration histories, from Task 6A specification

3.5.2 Calibration to flow

We perform the model calibration in the following manner:

1. Pipes length and orientation;
2. Acting on the pipe conductivities and apertures.

The flow calibration is performed by trial and error, with the objective of reproducing as precisely as possible the piezometric response measured at the five boreholes. We chose to try reproducing the lowest drawdown values, which we believe to be the most representative. The calibration results are presented for the five boreholes on Figure 3-6 and Table 4-1. The calibrated heads are plotted over the model area on Figure 3-7.

The head variations we obtain show a very good agreement with the measured values. The only significant discrepancy concerns borehole KA3005A, which is located upstream of the injection well and is therefore less important for the modelling.

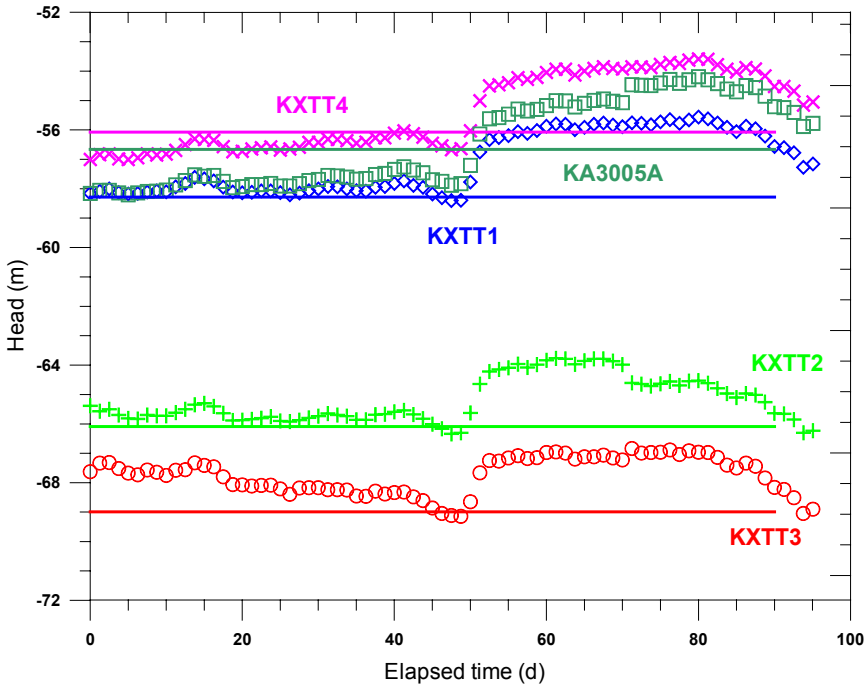

Figure 3-6 measured and calibrated hydraulic heads at the boreholes

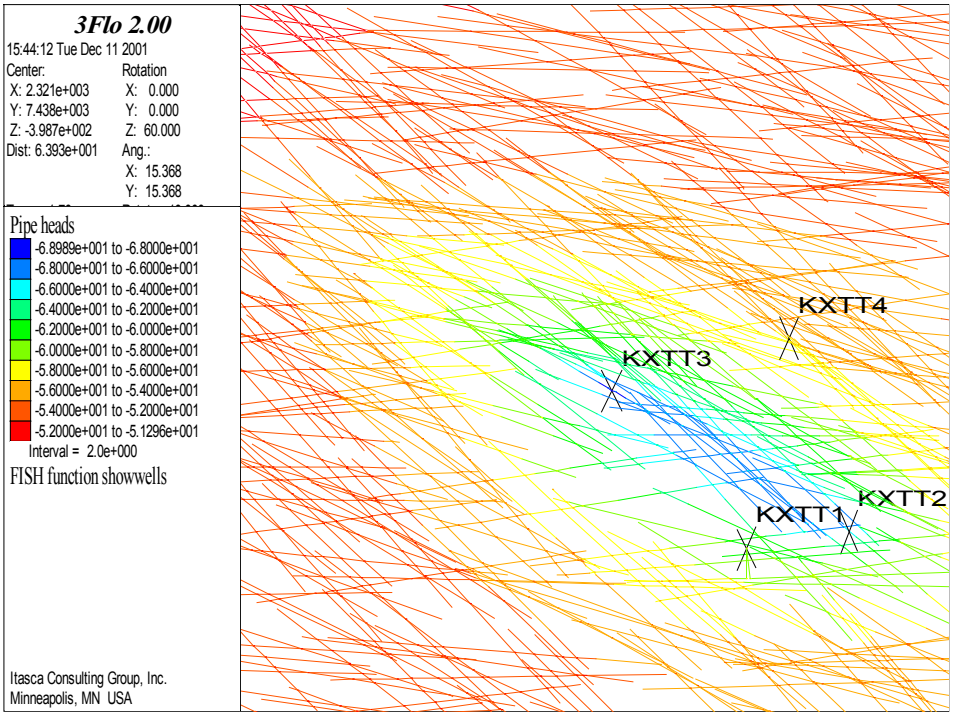

Figure 3-7: Task A -calibrated hydraulic heads over the network (m)

The pipe properties calibrated are listed in Table 3-6. The distribution of hydraulic conductivity *C* follows a lognormal probabilistic law. The resulting conductivity distribution is truncated at a minimum value equaling the mean value times 0.01.

Zones	Mean *C* (m^3/s)	Standard deviation (m^3/s)	Minimum C (m^3/s)
Highly conductive unit	$8\ 10^{-6}$	$8\ 10^{-6}$	$8\ 10^{-8}$
Rest of the model area	$7.5\ 10^{-8}$	$3.75\ 10^{-8}$	$7.5\ 10^{-10}$

Table 3-6 calibrated pipes hydraulic properties

If we assign a unit gradient between 2 opposite edges of the model and capture the total flowrate, we can compute the resulting global model transmissivity:

$$\mathbf{T = 2.8 \times 10^{-7}\ m^2/s}$$

This value is close to those obtained by the Task 4 modelling groups (Elert and Svensson, 2001).

3.5.3 Non-sorbing tracer breakthrough curve calibration

Our conceptual model for the channels is that of "ribbons", with a set width and a varying section and thickness. We use the cross section as the ratio between flowrates (uniquely defined by the flow-calibrated conductivities) and the advective velocities: we do not introduce any extra "tortuosity" factor. The pipe cross section A and the hydraulic conductivity C are correlated according to the law:

$$A = b.C^{1/2}$$

Where b is a calibrated coefficient.

Another parameter influences travel times: the longitudinal dispersion coefficient in the pipes, α. It is considered as homogeneous throughout the pipe network and is a second calibration parameter.

We then need a parameter akin to the flow wetted surface. This is done by specifying a further calibration parameter: the mean channel width. This enables us to compute channel thickness and thus governs the flow-wetted surface and the exchange of tracer between the flowing pore space and the immobile, diffusive pore space.

Finally, a diffusion coefficient is set for each zone in the immobile pore space. Note that for Iodine, we consider that due to the presence of clay material in the gouge, anion exclusion prevents its diffusion into the gouge. Therefore Iodine is only allowed to invade mylonite and diorite.

Note that we are constrained in the way we vary these various fitting parameters: we want their values to stay inside a realistic range, as close as possible from the estimates given. For example, the pipe apertures shall remain consistent with the magnitude of the estimated physical aperture of the fracture (1-3 mm).

The coefficient b has finally been set to 1.75 $(ms)^{1/2}$ and the mean channel width to 0.92 m. Note that this is obviously not the actual width of preferential flow channels in the fracture plane, since such channels would largely overlap each other. Real channels

have heterogeneous apertures, yielding the same "conductivity to surface area" ratio with lower widths. The resulting channel apertures have a mean of 6 10^{-4} m and a standard deviation of 7.3 10^{-4} m. Most apertures are contained in the lower range of the estimated fracture apertures, between 0.4 and 1 mm (Figure 3-8) with a few thicker channels (up to 9 mm thick) corresponding to the highly transmissive zone, as discussed above.

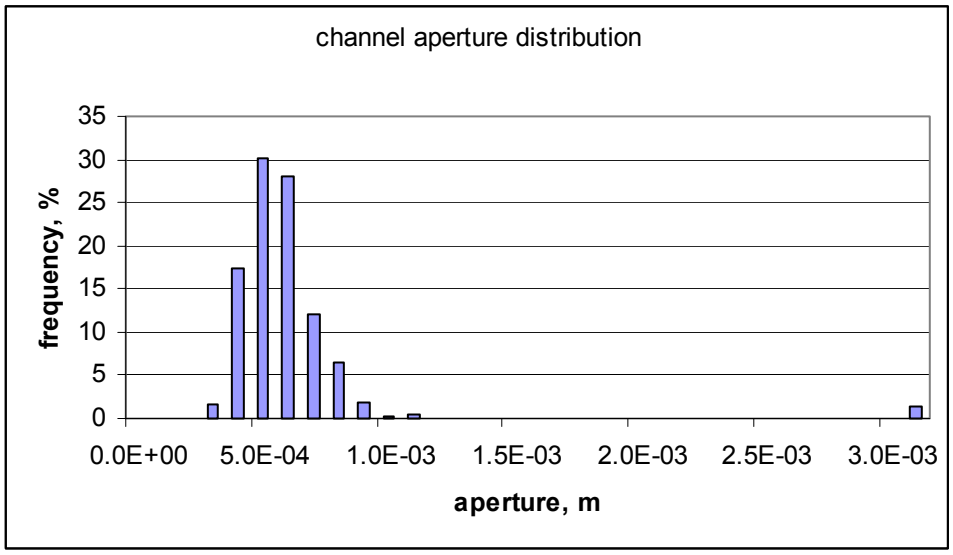

Figure 3-8 Channel aperture distribution

The coefficient of dispersivity has initially been set at a value of 1 m. In order to match the early portion of the non-reactive species breakthrough curve, we progressively decreased this coefficient, during the calibration process, down to a value of 0.2 m. Note that the perfect mixing at the pipes intersections adds a "dispersive effect" that could explain this low value. One result we obtained is unexplained: in order to match the Co breakthrough curve, we had to use for that tracer a coefficient of dispersivity of 0.5 m. This may be an effect of varying boundary conditions during the test, as reported by (Andersson *et al.*, 1998): although the Cobalt was injected at the same time as the less reactive tracers, because it stayed longer in the network it was subjected over its travel time to boundary conditions differing from the initial ones.

The diffusive properties are taken from the specification, and then modified in order to improve the breakthrough calibration. We try to keep the same values for most tracers, as illustrated by the parameter tables (see paragraph 3.4 above), and assign effective diffusivity values to the three materials we consider (diorite, mylonite, and gouge) proportional to their porosity. We end up with effective diffusivities of 10^{-14} m^2/s in diorite and mylonite, and of 2.10^{-12} m^2/s in gouge, except for Iodine, for which we double these values. The porosities of the materials are: 0.1% for diorite and mylonite, and 20% for gouge. We consider that channels are coated with 2 mm thick mylonite on 60% of their surface, and with 1 mm thick gouge on 20% of their surface (see Figure 3-4). On the remaining 20% of the surface area, diorite is directly in contact with the flowing porosity.

3.5.4 Sorbing tracer breakthrough curve calibration

The remaining parameters that describe retardation effects are the rock density (taken at 2,700 kg/m^3), and the Ka's and Kd's for the various materials and tracers. We try to limit the number of calibration parameters, by using only one Ka for each tracer (i.e. we use a "lumped" Ka that accounts for all fracture surface retardation). We start up with a value of Ka (in m) equal to the Kd value (in m^3/kg) for diorite, except for Co (ratio of 10 between Ka and Kd). In this, we simply follow the indications in the task specification.

Compared to the values specified, we need to change some parameters for the diorite retardation in order to get a satisfactory fit:

- For Sr, we keep Kd unchanged, but decrease Ka to 10^{-7} m.
- For Co, we need to multiply Ka and Kd by 6 (keeping a ratio of 10 between the two) from (8.10^{-3} m; 8.10^{-4} m^3/kg) to (5.10^{-2} m; 5.10^{-3} m^3/kg).

The Kd factors for mylonite are fitted to a value close to the ones for diorite, except for Sr, for which we need a larger retardation (factor or 10). Kd's in gouge are set to one hundred times the Kd's in mylonite, except for Tc and Am where we use only a factor of 10.

3.6 Adapting the model for large time scales

The model boundary conditions are modified as indicated in the task specification, for both task 6B and task 6B2. All material properties and distributions are unchanged.

For task 6B, the observed flow field must be modified in such a way that the pressure gradient between the injection and the extraction wells is in the order of 0.1%, and the background flow field must be modified in order to account for the absence of the tunnel impact and therefore prescribe an hydraulic gradient oriented from KXTT1 towards KXTT3. Note that the general structure of the flow field stays essentially the same: radially convergent test.

The same flow path and material properties are assumed for Task 6B as in Task 6A.

The problem is therefore the following: how can we move from the Site Characterization model (Task A) to a Performance Assessment approach (Task B)? Beside the adjustment of hydraulic boundary conditions (i.e. inverting the flow field and decreasing the magnitude of the gradient), we chose to simplify the system by removing all pipes which are not located downstream of the injection well and upstream of the recovery well (6A/B) or line (6B2). Note that this is done after the head field has been computed for the whole network, and fixed. In this way, removing some part of the network does not impact on the flow field in the remaining part of the network.

The reasoning behind such a simplification is the following: except for the part of their jump representing longitudinal diffusion, particles, at any time, travel either downstream (if they are in the fracture) or normally to the flow (if they are in any matrix block). If we disregard longitudinal diffusion, any particle originating at the injection well can visit only the pipes, which are downstream from it. In the same manner, the flow field and tracer test configurations we impose here mean that the tracer has no choice but leaving the model through the pumping well (Task 6A, 6B) or through the downstream fracture (Task 6B2). We therefore know that any pipe visited

by a particle is upstream from the recovery well or line. It follows that, barring the upstream jumps that are required to simulate longitudinal dispersion, the only pipes that may be visited by particles in our model are the ones downstream of the injection well and upstream of the recovery well or line.

We take into account the possible occurrence of upstream jumps by keeping "cushion pipes", i.e. pipes in the original network that are directly upstream of any selected pipe. In this way, particles that are trying to go upstream on the border of the selected pipe network will be able to travel some distance (i.e. the length of the cushion pipe). Note that we may still encounter problems if the upstream distance a particle is supposed to travel is longer than the length of the cushion pipe it has entered. In such a case the particle will leave the network at the upstream end of this pipe. In order to make sure our simulation is not biased in this way, we check where all particles leave the model during the simulation. In all the simulations presented in this report, no particle leaves the network at the upstream end of a cushion pipe.

Figure 3-9 shows the resulting Task B network, including the pipes representing the injection and the extraction wells. Note also on the figure the presence of the "cushion pipes used to enable dispersion/diffusion of tracer upstream.

We account for the new conditions by lowering and reversing the pressure gradient prescribed at the model boundary. The KXTT3 extraction flowrate has also been lowered to 10^{-8} m^3/s (i.e. 0.6 ml/min).

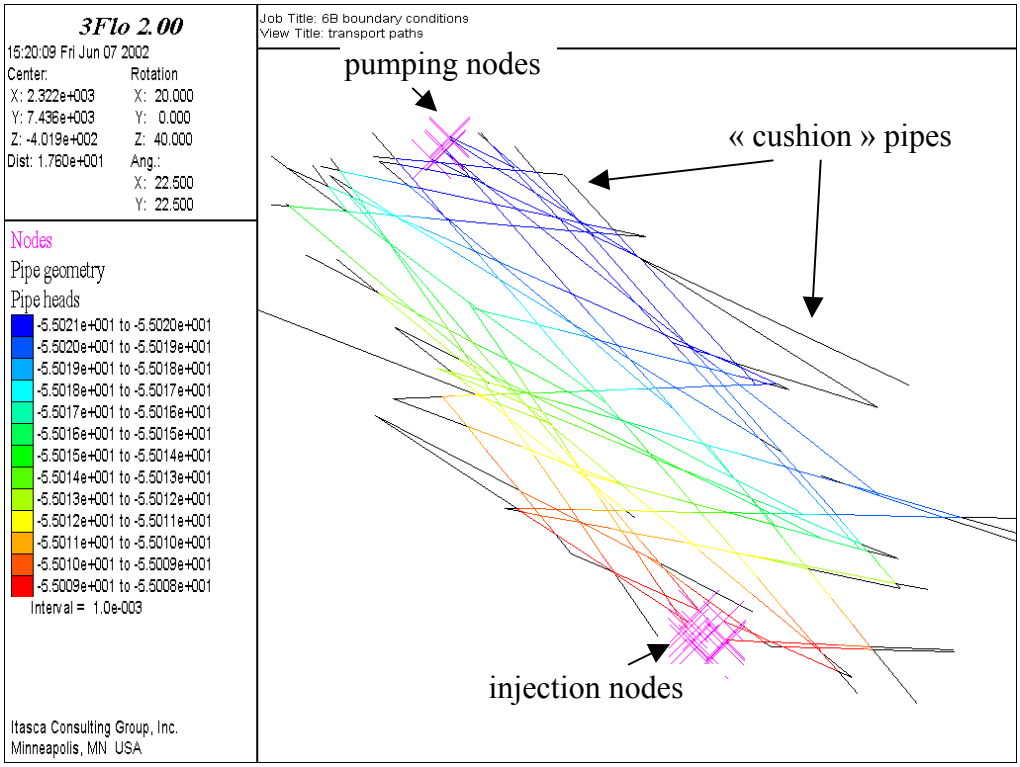

Figure 3-9 Task 6B boundary conditions. Heads in the simplified network

For task 6B2, the flow field is modified to better represent the long term conditions around a waste canister, as illustrated earlier (Figure 2-2): the tracer is injected along a line instead of a single borehole intercept, and flow is due only to a small "background" gradient, without any radial effect due to pumping. Tracer is "collected" down gradient

along a line that mimics the presence of a fracture intersection. Flow and transport properties are unchanged.

Using the same network-simplifying algorithm as for the task 6B conditions, we obtain the simplified network shown in Figure 3-10. As can be readily seen, the number of pipes that may be visited by a tracer released at the injection nodes is much larger, when compared with the 6B case (Figure 3-9). The 6B2 boundary conditions allow a more "distributed" sampling of the fracture by the tracer than the radially converging 6B boundary conditions.

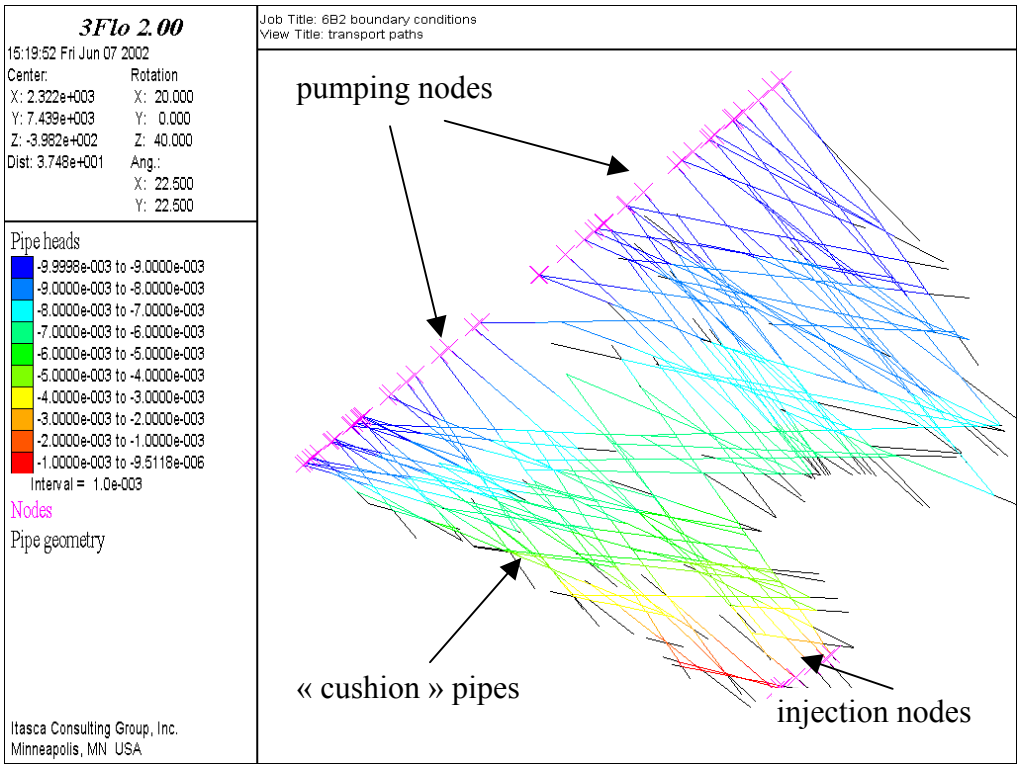

Figure 3-10 Task 6B2 boundary conditions. Heads in the simplified network

4 Results - Performance measures

4.1 Task 6A

4.1.1 Drawdown in injection and pumping borehole

As discussed in part 3.5.2, the calibrated heads at boreholes are quite close to the measured ones, due to a carefull flow calibration.

Simulated heads, meters					
	KXTT1	KXTT2	KXTT3	KXTT4	KA3005A
"natural"	-5.30E+01	-5.29E+01	-5.28E+01	-5.30E+01	-5.35E+01
pumping	-5.83E+01	-6.61E+01	-6.90E+01	-5.61E+01	-5.67E+01
drawdown	5.26E+00	1.32E+01	1.62E+01	3.09E+00	3.22E+00

Table 4-1 Heads simulated in the 5 borehole intercepts, task 6A

4.1.2 Breakthrough time history for the tracers

Here also, due to the calibration, Figure 4-1 shows a very good fit between the measured and simulated values. Note the –3/2 log-log slope of the breakthrough curves for Cobalt, Technetium and Americium after approximately 1 year, and for Strontium after about 0.1 year : we can infer from this that within the framework applied here, diffusion to the matrix is playing a significant role in the shape of the breakthroughs, even for these "short term" runs already.

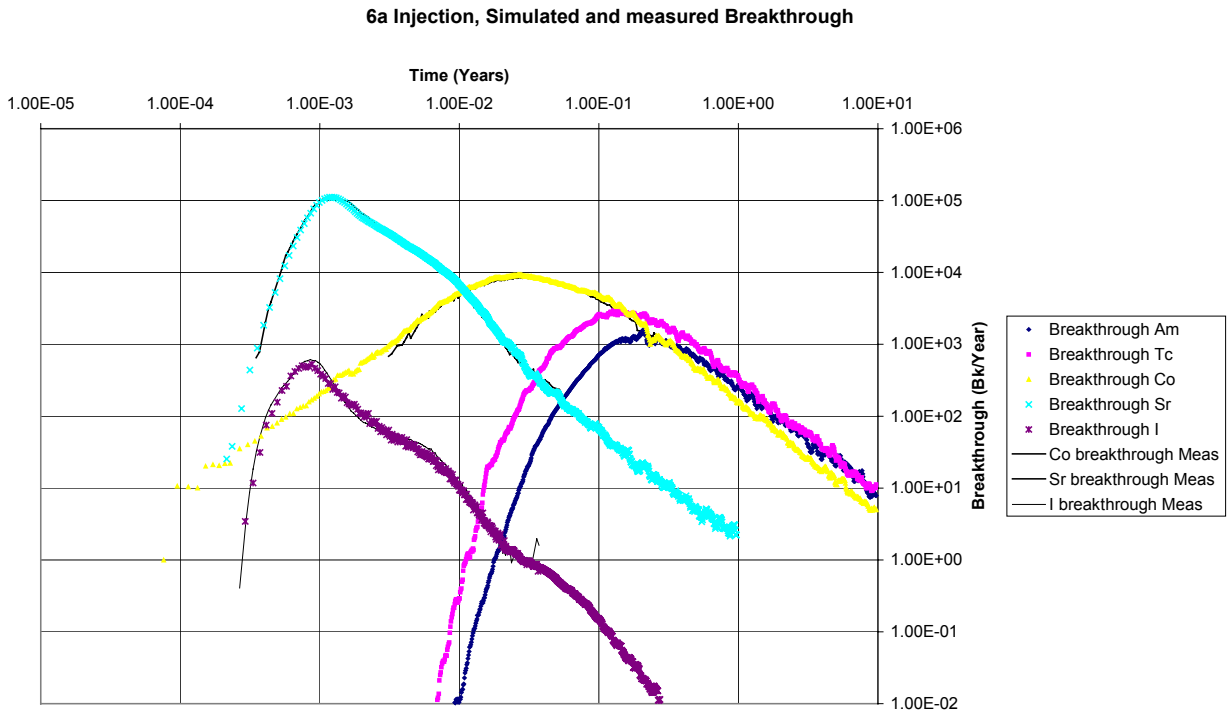

Figure 4-1 Breakthrough curves for measured injection curves, 6A

Note that the simulations were interrupted at the 10-year limit. At that time, for the most sorbing tracers, not all the tracer injected was recovered. Therefore, some of the 50% and 95% recovery times could not be computed. For the sake of completeness, we add a line in the recovery times table, displaying the % recovery at the final time of the simulation. In Table 4-2, for example, only Sr and I show full recovery after 10 years, while Am, Tc and Co are recovered only 29%, 47% and 49% respectively. Note that the results for Tc show a peak at about 55 days (0.15 year), and are therefore not compatible with the absence of recovery noted during the real testing. This will be investigated in the sensitivity study (paragraph 4.4.3).

6A, Real Injection, time in years					
Recovery	**Am**	**Tc**	**Co**	**Sr**	**I**
5%	2.23E-01	1.26E-01	2.77E-02	9.90E-04	6.42E-04
50%	-	-	-	3.29E-03	1.79E-03
95%	-	-	-	9.73E-02	3.19E-02
% recovered after 10 years	29	47	49	100	100

Table 4-2 Breakthrough times for recovery of 5%, 50% and 95% of the injected mass, and % recovered at the end of the simulation, 6A

As could be expected, the breakthrough curves obtained from the simulation of a Dirac pulse (Figure 4-2) are more regular than the ones obtained from the real injection sequence. Except for Iodine (for which the time scale is such that diffusion to the matrix is not allowed enough time to become significant, all the tracer being recovered within about one day), all tracers show toward the end of the simulation the characteristic "diffusion controlled" -3/2 log-log breakthrough slope.

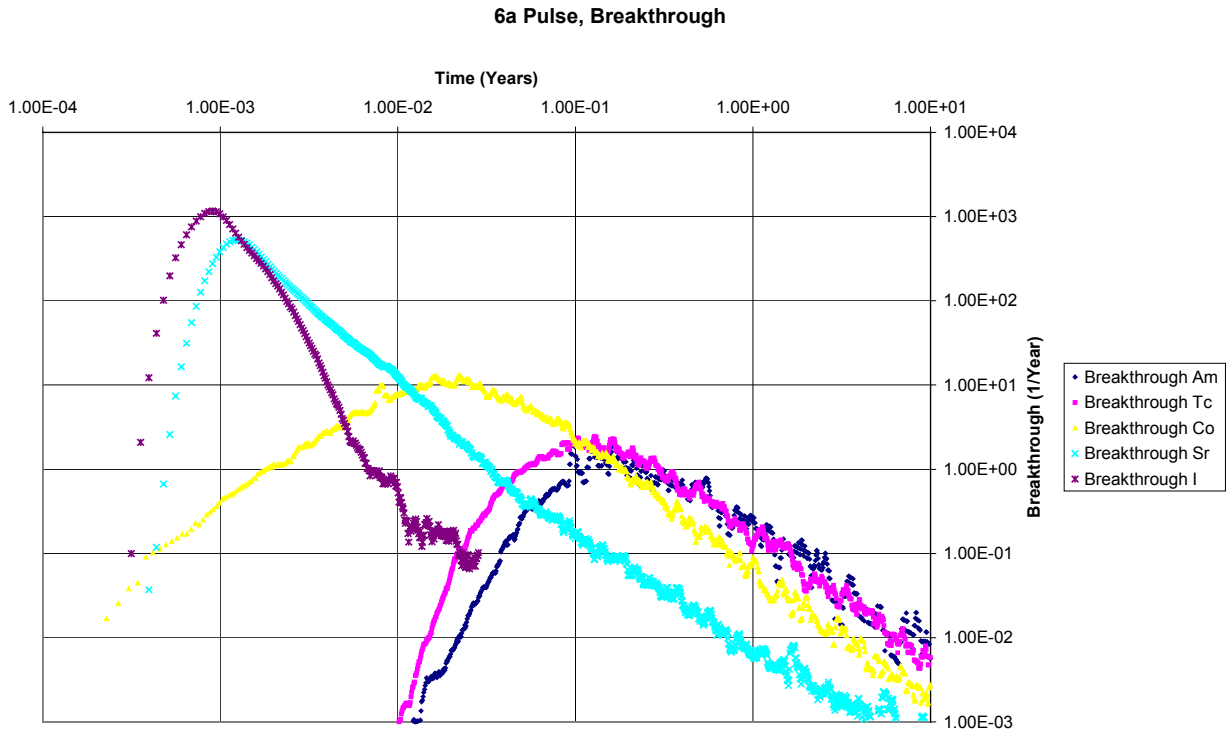

Figure 4-2 Breakthrough curves for Dirac pulse injection, 6A

6A, Pulse, time in years					
Recovery	**Am**	**Tc**	**Co**	**Sr**	**I**
5%	1.15E-01	7.73E-02	1.14E-02	9.90E-04	7.27E-04
50%	8.11E-01	4.52E-01	7.50E-02	2.16E-03	1.08E-03
95%	-	-	3.27E+00	6.29E-02	2.81E-03
% recovered after 10 years	86	92	100	100	100

Table 4-3 Breakthrough times for recovery of 5%, 50% and 95% of the Dirac pulse injection, and % recovered at the end of the simulation, 6A

4.1.3 Maximum release rate

The maximum release rates for the real injection history depends on the amount of tracer injected. This explains the much lower rate obtained for Iodine, as the ”concentration” (in Bq) of this tracer at injection was much lower (see Figure 3-5). The maximum release rate for the pulse injection is divided by a factor close to 1000 from Iodine to Americium. This is also apparent in Figure 4-2. Clearly, for this scale of travel times, Iodine and Strontium behave in a similar manner at peak (with a maximum release rate for Strontium equal to almost one half of the rate for Iodine), then retention of Strontium brings it closer to Cobalt, which shows an intermediate behaviour, while Technetium and Americium show responses almost identical in shape, if not in time scale.

6A, Real Injection, Rate in Bq/year				
Am	**Tc**	**Co**	**Sr**	**I**
1.60E+03	2.94E+03	9.24E+03	1.11E+05	5.30E+02

Table 4-4 Maximum release rate using measured injection curves, 6A

6A, Pulse, Rate in Bq/year				
Am	**Tc**	**Co**	**Sr**	**I**
2.08E+00	2.44E+00	1.29E+01	5.28E+02	1.17E+03

Table 4-5 Maximum release rate using Dirac pulse injection, 6A

4.2 Task 6B

4.2.1 Breakthrough time history for the tracers

Figure 4-3 and Figure 4-4 show the breakthrough time histories for the two types of injection specified for task 6B: constant injection (10^6 Bq/l concentration), and injection of a unit pulse at time 0. Only Iodine and Strontium breakthroughs are complete after 10^6 years, while a large part of the mass of the other tracers is still retained in the matrix. Here, the responses of Cobalt, Technetium and Americium are similar, while Strontium shows an intermediate response and Iodine features a much faster and sharper (i.e. larger peak values) response.

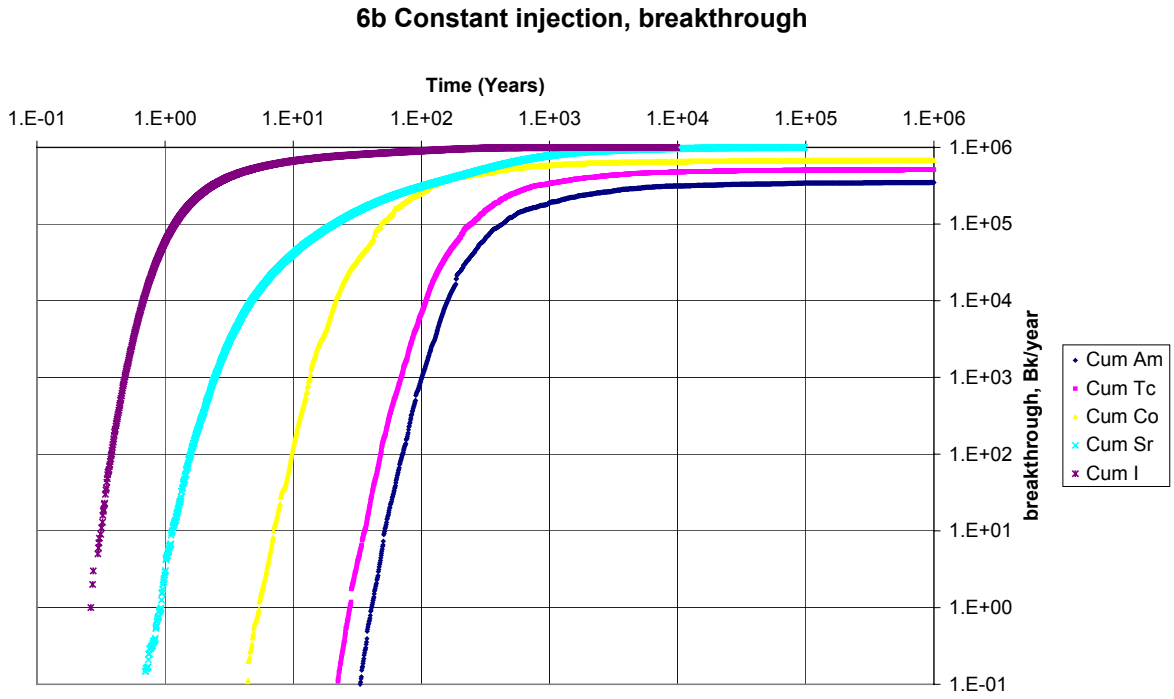

Figure 4-3 Breakthrough curves for constant injection rate, 6B

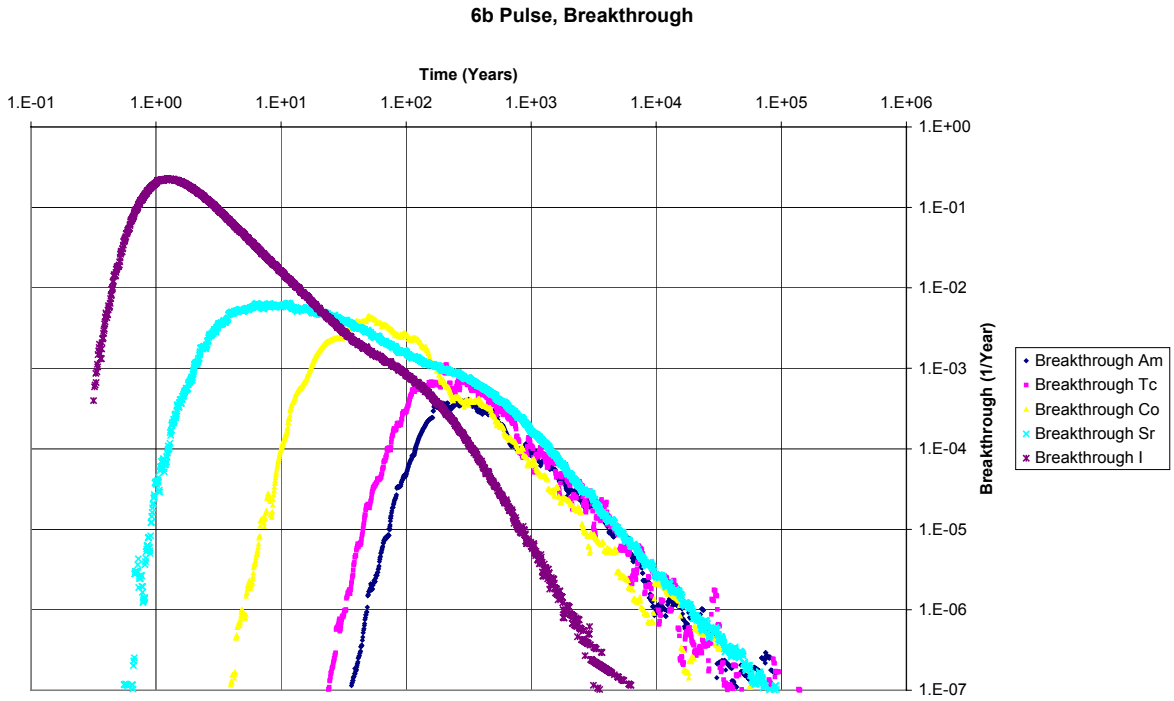

Figure 4-4 Breakthrough curves for Dirac pulse injection, 6B

6B, Pulse, time in years					
Recovery	**Am**	**Tc**	**Co**	**Sr**	**I**
5%	2.77E+02	1.76E+02	3.84E+01	1.15E+01	9.59E-01
50%	-	6.32E+04	4.28E+02	2.83E+02	4.39E+00
95%	-	-	-	6.55E+03	1.90E+02
% recovered after 10^6 years	35	51	67	100	100

Table 4-6 Breakthrough times for recovery of 5%, 50% and 95% of the Dirac pulse injection, and % recovered at the end of the simulation, 6B

4.2.2 Maximum release rate

Maximum release rates for the five tracers during the 6B pulse simulation are given in Table 4-7. Here, because of the advection time scale, retention starts playing a role for Strontium long before the peak. Consequently, the ratio of the release rates for Strontium and Iodine decreases from about ½ in case 6A to about 3% in case 6B. Other maximum release rates stay approximately in the same ratios: 1-2 % for Co, 0.3-0.5 % for Tc, 0.15-0.2 % for Am.

6B, Pulse, Rate in 1/year				
Am	**Tc**	**Co**	**Sr**	**I**
4.12E-04	1.11E-03	4.45E-03	6.48E-03	2.29E-01

Table 4-7 Maximum release rate using Dirac pulse injection, 6B

4.3 Task 6B2

4.3.1 Breakthrough time history for the tracers

Figure 4-5 and Figure 4-6 show the breakthrough histories for all tracers with the 6B2 boundary conditions, respectively for constant injection (10^6 Bq/l concentration), and for injecting a unit pulse at time 0. Here again, only Iodine and Strontium breakthroughs are complete after 10^6 years.

Note that the Cobalt response seems to be anomalous here, with a peak (in Figure 4-6) sharper than expected, reaching higher than the Strontium values. Technetium and Americium also show sharper breakthrough curves, while Iodine and Strontium show a shift in arrival times by a factor of 5 to 10 compared to the task 6B values illustrated in Figure 4-4.

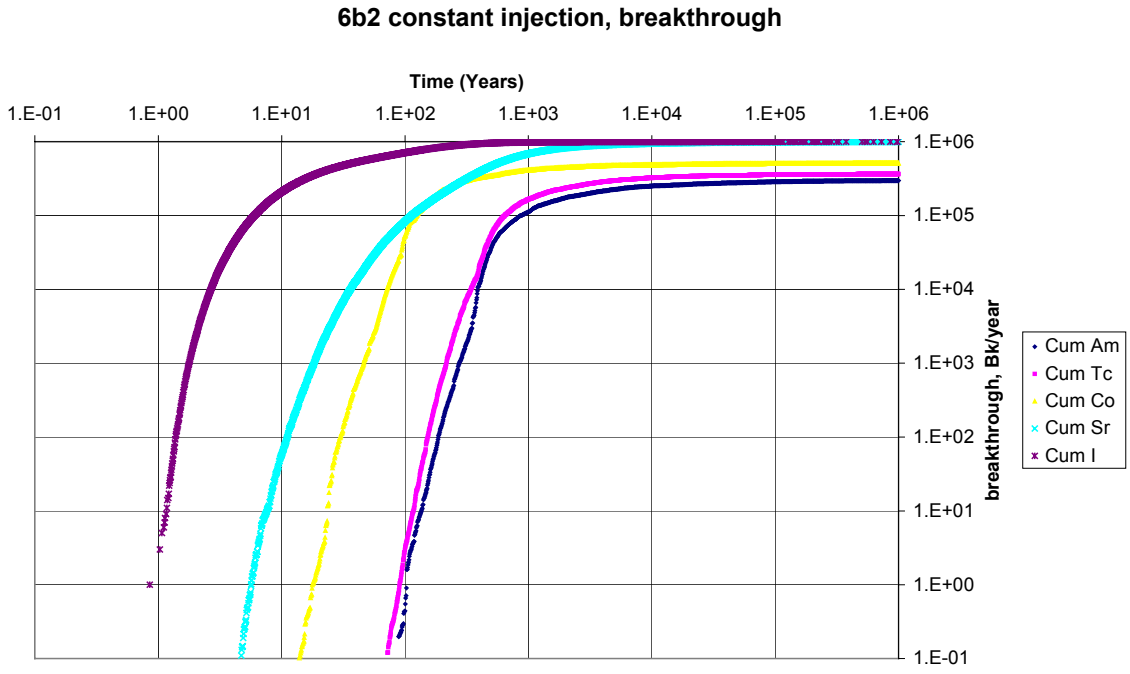

Figure 4-5 Breakthrough curves for constant injection rate, 6B2

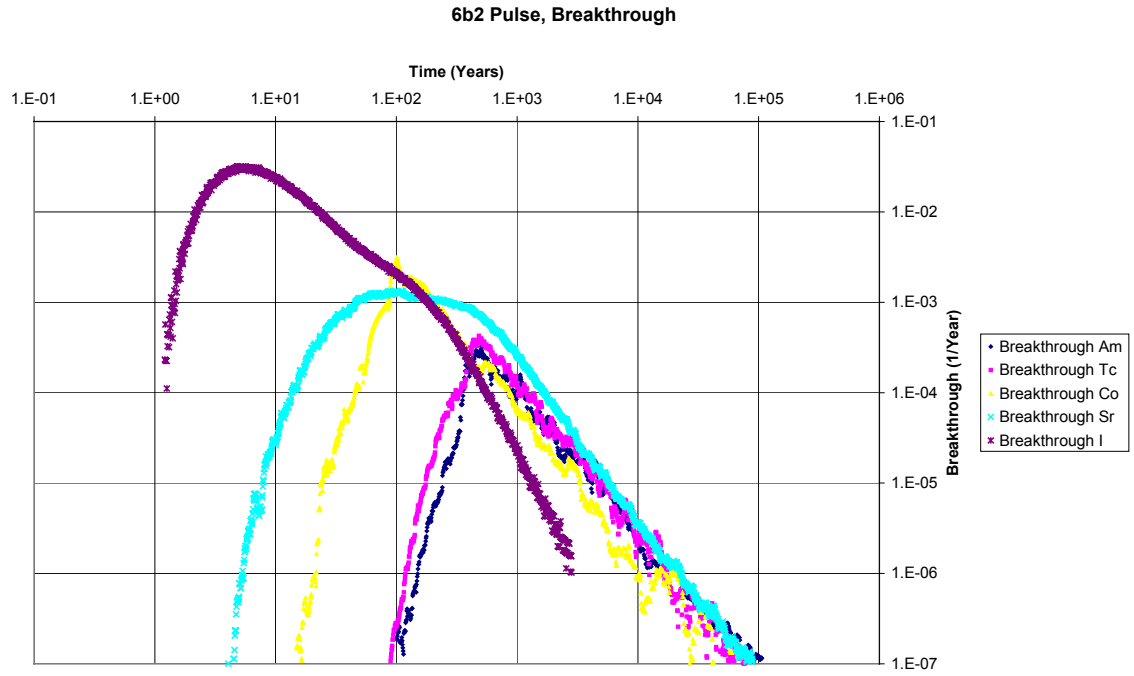

Figure 4-6 Breakthrough curves for Dirac pulse injection, 6B2

6B2, Pulse, time in years					
Recovery	**Am**	**Tc**	**Co**	**Sr**	**I**
5.00E-02	5.50E+02	4.89E+02	9.92E+01	7.37E+01	4.36E+00
5.00E-01	-	-	3.81E+04	5.47E+02	3.53E+01
9.50E-01	-	-	-	1.12E+04	4.50E+02
% recovered after 10^6 years	30	36	51	100	100

Table 4-8 Breakthrough times for recovery of 5%, 50% and 95% of the Dirac pulse injection, and % recovered at the end of the simulation, 6B2

4.3.2 Maximum release rate

Maximum release rates for the five tracers during the 6B2 pulse simulation are given in Table 4-9. The rates are about 1/10 of the 6B ones for Iodine and Strontium, while they are almost unchanged for the more sorbing tracers. A tentative explanation would be that at the time scales involved, diffusion and retention totally govern breakthrough times for the latter, while the hydraulic boundary conditions still have a strong effect on the release of Iodine and Strontium.

6B2, Pulse, Rate in 1/year				
Am	**Tc**	**Co**	**Sr**	**I**
3.26E-04	4.25E-04	3.12E-03	1.33E-03	3.20E-02

Table 4-9 Maximum release rate using Dirac pulse injection, 6B2

4.4 Sensitivity studies

4.4.1 Effect of spatial variability

We check the effect of the spatial variability of the pipe properties for two contrasting tracers, i.e. I and Am. For both tracers, we use 6B and 6B2 boundary conditions, giving a total of four cases. For each case we generate 100 different networks with the same statistical properties and look at the variability of the response. Note that all the statistical properties of the networks are identical for cases 6B and 6B2. Only the boundary conditions, and therefore also the simplification of the network, change. Figure 4-7 and Figure 4-8 show the results obtained for the (I, 6B) and (I, 6B2) simulations, while

Figure 4-9 shows, for both types of boundary conditions, the distribution of the 5% arrival times. Similarly, Figure 4-10 and Figure 4-11 show the cumulative breakthroughs we get for the (Am, 6B) simulations and (Am, 6B2) simulations respectively, while

Figure 4-12 shows the distribution of the 5% arrival times for Am, in both 6B and 6B2 cases Finally, Table 4-10 enables a comparison of the results, by looking at the mean and coefficient of variation of the 5% arrival times for the four cases studied.

These simulations highlight the effect of the individual positions and properties of the channels/flow paths on the overall response, versus the effect of the overall statistical properties. For example, if the response is dominated by local conditions at the injection point (6B boundary conditions) or line (6B2 boundary conditions), since the properties of the channels close to the injection are not conditioned, the variability in response should be relatively high. On the other hand, if the flow paths are long enough that an integrating effect is predominant, then the response should be dominated by the average properties of the networks, and should therefore not vary significantly from one realisation of the network to another. Note that here, by “local conditions”, we mean distances in the order of the correlation length mentioned in the specifications, i.e. 0.4 meter. In our model this corresponds to the average travel path along a channel between two intersections (see paragraph 3.1.3). It is thus the scale of heterogeneity in the model.

The overall variability of the response from one realisation of the network to another is quite small, with breakthrough curves that stay within a one order of magnitude wide span for 6B boundary conditions, and within essentially a factor of 2/2.5 for 6B2 boundary conditions, as shown by the figures below. Also, we note that the 6B2 boundary conditions, which entail a more evenly distributed flow field, tend to produce

less variability in response: since the tracer samples a larger part of the flow field, large local variations in properties are more ”blurred” once integrated in the full test response. This can also be noted from Table 4-10, with coefficients of variation for T 5%of about 0.4 (conditions 6B) and 0.24 (conditions 6B2).

The behaviour of Am and the behaviour of I differ largely, with early arrivals of I about 100 times faster than early arrivals for Am, and with Am being still significantly retained in the matrix after 10^6 years while I breakthrough is complete after 200 to 800 years in all cases. However, the variability in behaviour from realisation to realisation is similar between the two tracers.

We can conclude the following: the actual exact position of the channels constituting the flow paths has only a limited influence on the breakthrough times. The early time variability does not seem to depend on the retention properties of the tracer, for the time scales relevant to the tracer. It is more influenced by the flow conditions, which govern the number of channels visited by the tracer, and thus the integrating of the responses from the source to the sink. In this regard, the 6B2 boundary conditions, which are meant to be more representative of actual “post-closure” conditions around a canister, yield less variable responses.

If we consider late time response, the retention properties prevail, since a non-reactive tracer is fully collected, and therefore shows no variability, while the reactive tracer is still retained in the matrix, and yields cumulative breakthroughs at 10^6 years within a 1 to 5 range.

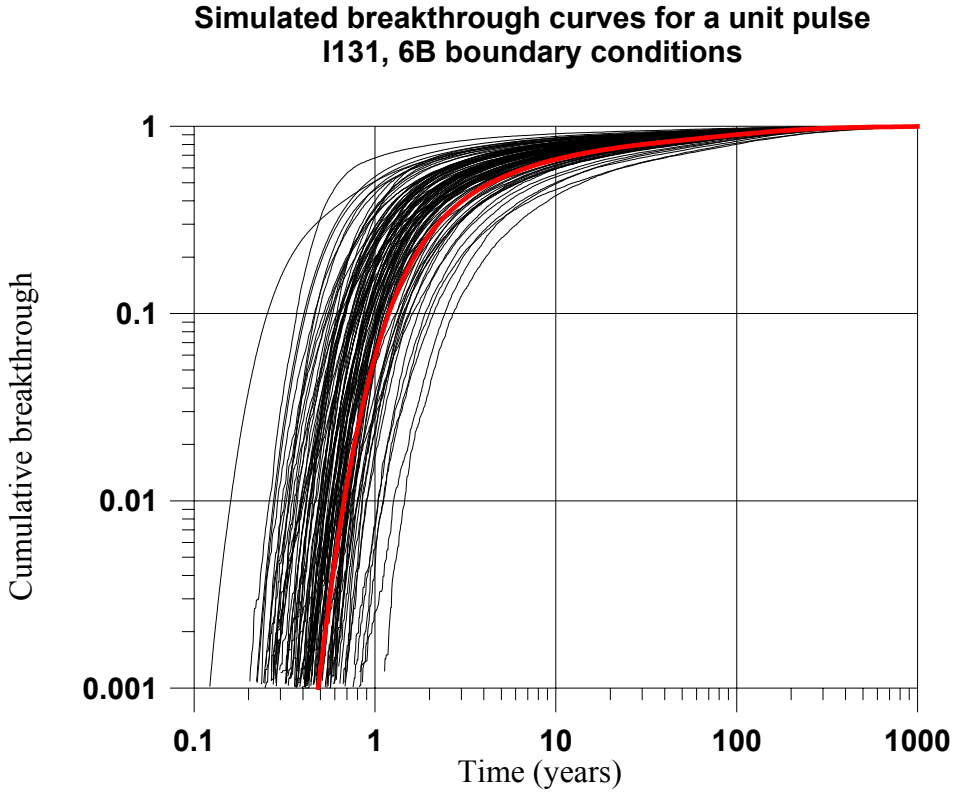

Figure 4-7 I131, 6B boundary conditions. Simulated cumulative breakthrough curves. Initial seed is red line.

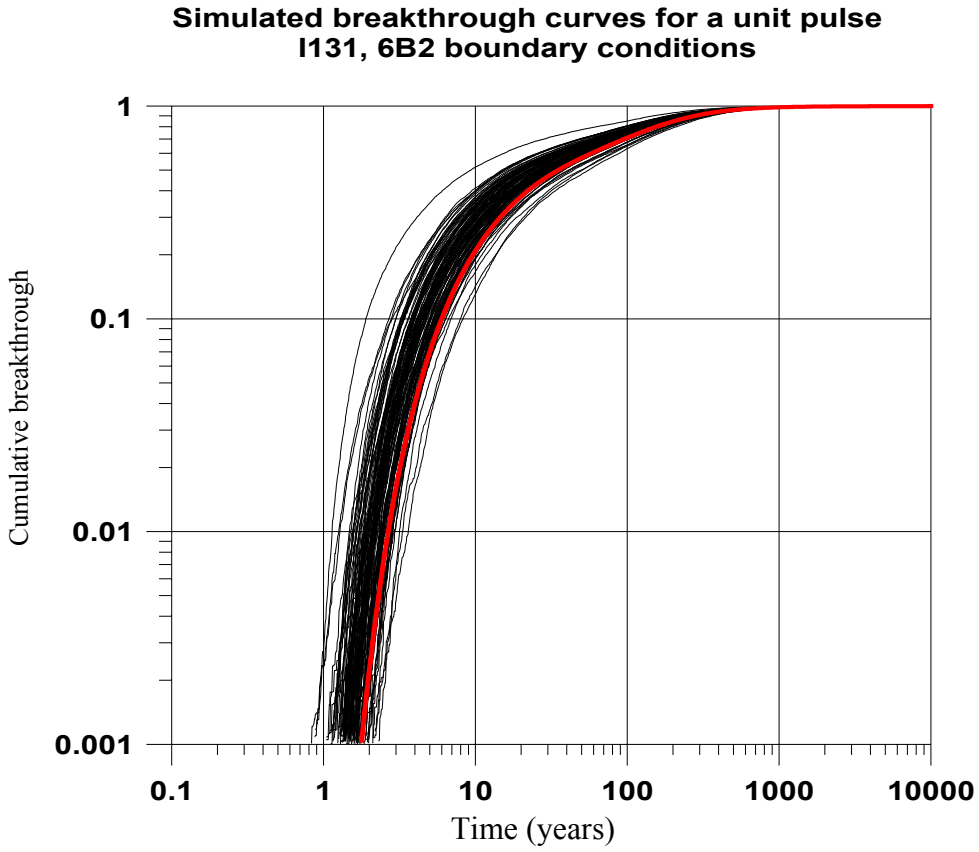

Figure 4-8 I131, 6B2 boundary conditions. Simulated cumulative breakthrough curves. Initial seed is red line.

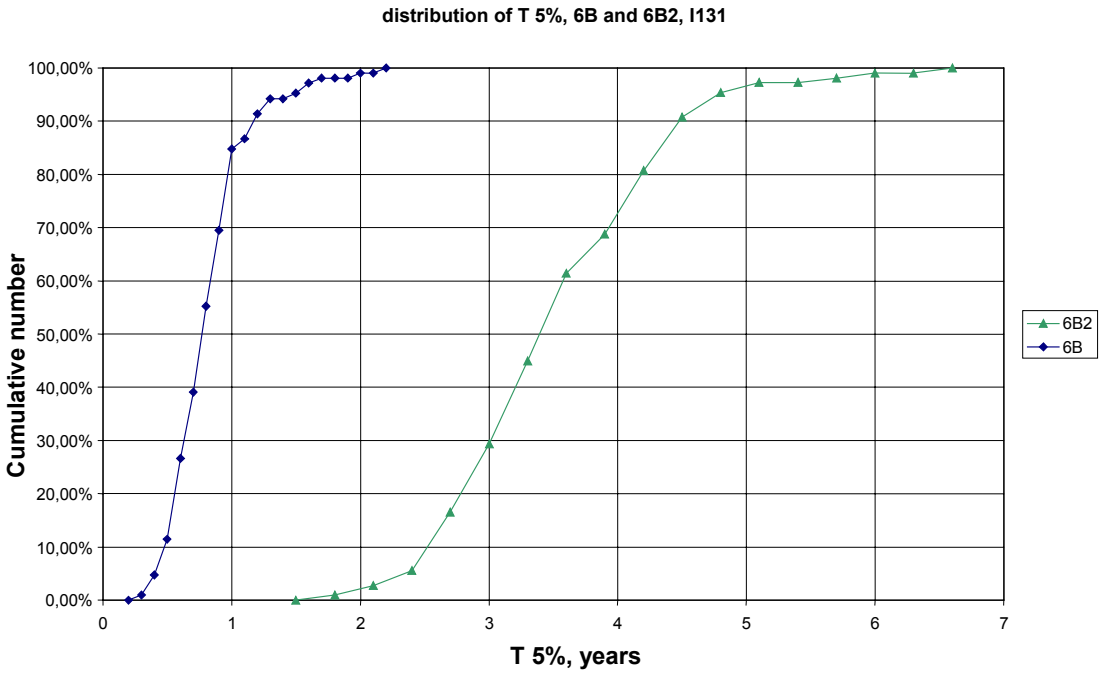

Figure 4-9 I131, 100 realizations. Distribution of T5%, 6B and 6B2 boundary conditions.

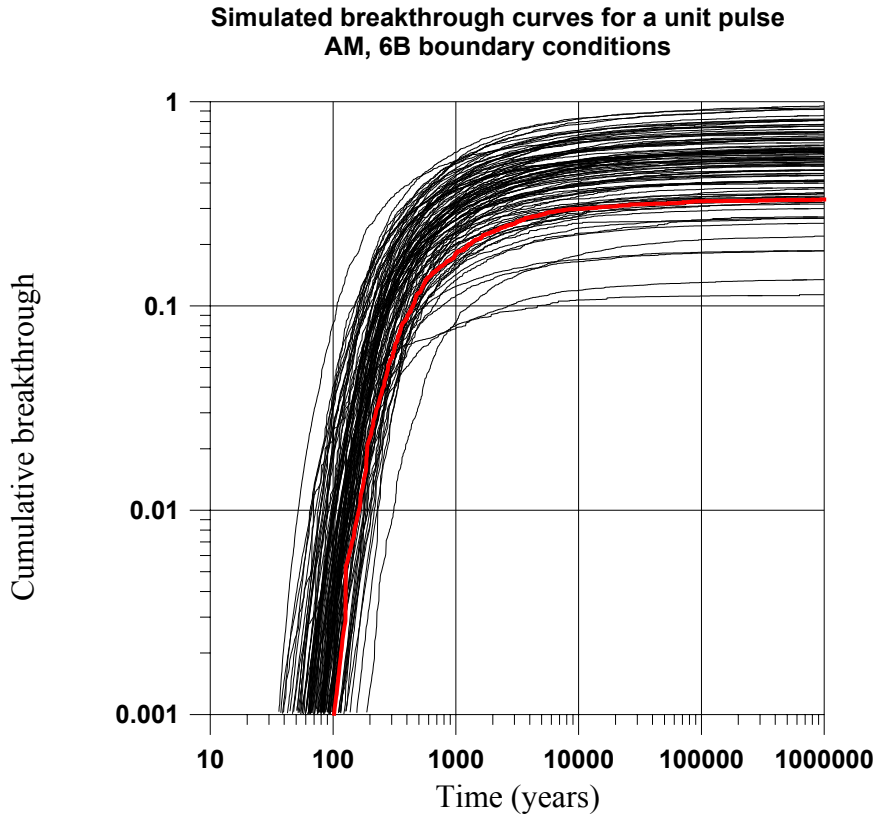

Figure 4-10 Am, 6B boundary conditions. Simulated cumulative breakthrough curves. Initial seed is red line.

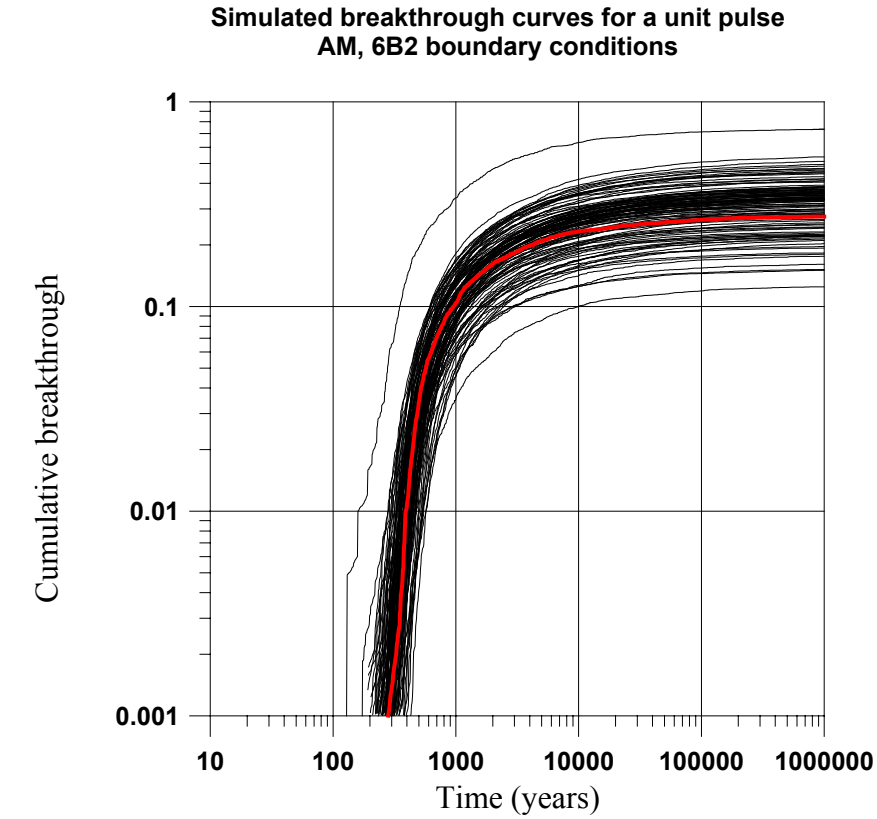

Figure 4-11 Am, 6B2 boundary conditions. Simulated cumulative breakthrough curves. Initial seed is red line.

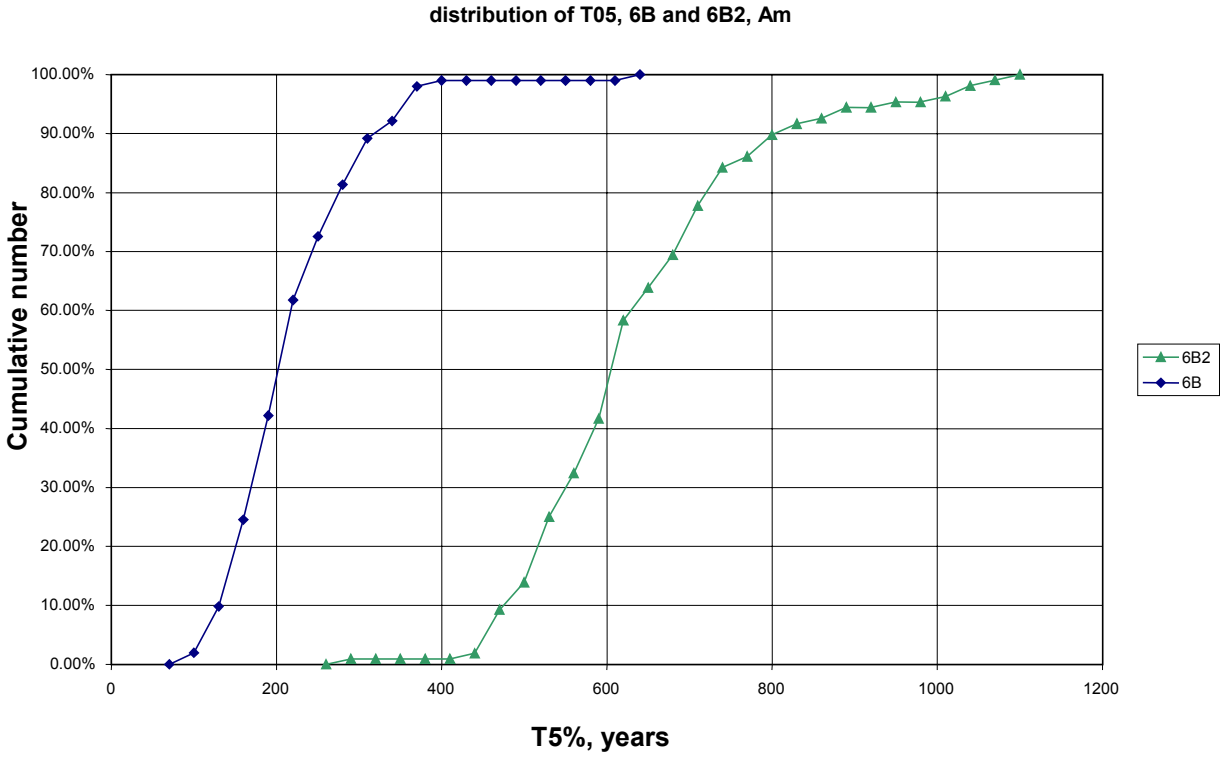

Figure 4-12 Am, 100 realizations. Distribution of T5%, 6B and 6B2 boundary conditions.

Tracer	Boundary conditions	Average T 5%	Coefficient of variation, T 5%
I	6B	0.81	0.40
	6B2	3.5	0.23
Am	6B	214	0.38
	6B2	637	0.25

Table 4-10 Distribution of T 5% for I131 and Am, 6B and 6B2 boundary conditions, 100 realizations.

4.4.2 Illustration of the effect of considering diffusion on the extrapolation in time

In a first phase of this project, simulations were run without taking diffusion to the matrix into account. Retardation was provided only by a linear surface retardation model. The following figures and table are part of this early effort, and are meant to illustrate the importance of the chosen conceptual model. The geometrical properties for the network, and flow-only properties, where identical to the ones used in the simulations reported above.

We reproduce here the results obtained for Strontium. Figure 4-13 shows the fitting we obtained for Sr using the task 6A boundary conditions. This fit is not as precise as the

one obtained when taking diffusion into account, as illustrated in Figure 4-1. However, this can still be considered as acceptable.

50 simulations were performed using the 6B and 6B2 boundary conditions and the fitted model properties. In the same way as before, the statistical properties of the 50 realisations of the network are identical. When looking at these long term predictions, the effect of the difference in conceptual model is striking, as shown in Table 4-11 giving the mean breakthrough times. The numbers we obtain there are only a fraction of the ones obtained with the previous calibration, with late arrival more than 1000 times earlier than in the main simulations (see Table 4-6 and Table 4-8).

This simple example illustrates the paramount importance of the conceptual model whenever properties are measured at a given scale (either in space or time) and then used at a larger scale. Here the extrapolation in time simply yields “opposite” results, with fast and complete arrivals in all cases, compared to the simulations exposed in the main body of this report.

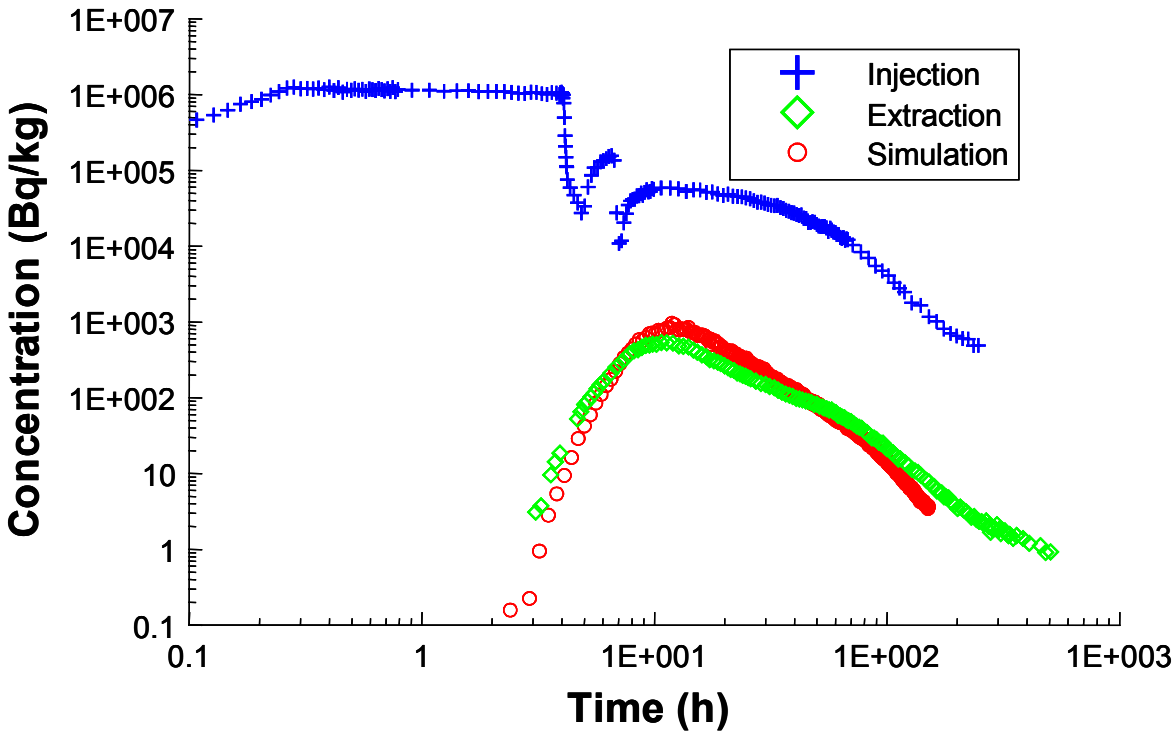

Figure 4-13 6A, Sr. Fitting without diffusion

6B and 6B2, Sr Pulse, time in years		
recovery	**6B**	**6B2**
5.00E-02	1.03	3.67
5.00E-01	2.03	6.41
9.50E-01	4.38	11.86

Table 4-11 Breakthrough times for recovery of 5%, 50% and 95% of the Dirac pulse injection of Sr, 6B and 6B2 boundary conditions, model without matrix diffusion.

4.4.3 Assessment of Tc behaviour by coupling transport and speciation

4.4.3.1. Introduction

The reactivity of some of the injected tracers calls for questions on the linearity of the retention processes. To address this problem, it is important to try to identify the main mechanisms that control this retention in order to assess the eventual limits of the linearity assumption.

Among the various tracers injected, ^{99m}Tc and ^{58}Co are the two most likely candidates for undergoing a non-linear retardation. In fact, both tracers proved problematic, when trying to finalize the task 6A simulations: fitting Co required modifying the dispersivity compared to other tracers, while the simulations predicted for Tc a breakthrough that in fact was not observed. We chose to model the Tc injection, in order to check a possible explanation for the absence of a breakthrough.

A major complication arises from an on-site change of hydraulic and geochemical boundary conditions, due to the drilling of a borehole at 200 m south-west of the TRUE-1 site (Andersson *et al.*, 1998). Beside its consequences on the flow field, this event caused a drop in the electrical conductivity and in Ca concentrations during the experiments (Winberg *et al.*, 2000), which introduces a trend in the long term experimental data. For instance, one can expect the sorption of the reactive tracers to be gradually increased because of the lesser competition with calcium for the surface sites. The observed changes of head difference between the pumping and the observation sections (Andersson *et al.*, 1998, fig. 3.11) may also increase the dilution of the injected solution. Accounting for those changes is difficult. However, because Tc has a high reactivity, it is likely to interact with the fracture sides or precipitate in a short time span. We therefore avoid representing the changes of hydraulic and geochemical boundary conditions during the test, but limit ourselves to simulating the first weeks after the start of the injection.

Winberg *et al.* (2000) list the *Feature A* water composition. The identification of both pyrite and reduced iron and sulphur in the medium indicates a reducing geochemical environment that may affect the fate of redox sensitive reactive compounds like Tc. For the experiments, ^{99m}Tc is injected as the anionic TcO_4^- Tc(VII). Note that in an oxidizing environment, TcO_4^- Tc(VII) would not undergo any significant retardation and therefore would be recovered at the pumping well. Here, the reducing environment

has probably transformed Tc(VII) into Tc(IV) which can more readily be adsorbed or precipitated as oxides or sulfides. Such a behaviour explains the Tc retention.

In this paragraph, we present some simulations coupling transport and speciation that aim to provide some scenarios of the Tc retardation and the potential limits of a "*Ka – Kd"* approach.

4.4.3.2. The geochemical model

We adjusted the total concentrations of the major chemical elements in order to try to reproduce the initial conditions (*i.e.* the pore water concentrations). The thermodynamic constants are taken from the *EQ3/6* data base (Wolery, 1992) and all reactions are assumed to be at equilibrium. The minerals considered here are restricted to the following list: pyrite, hematite, calcite, TcS_2 and $TcO_2,(H_2O)_2$(am).

The main results are displayed in Table 4-12. The computed pH is 7.40 (the observation is between 7.4 and 7.6) and the calculated redox potential of the pore water is: -169.7 mV (reliable on-site measurements are generally very difficult to obtain).

The solution is at equilibrium with respect to calcite, pyrite and hematite, which reflects the on-site observations.

The injected solution is assumed to be made of *Feature A* groundwater, which has been opened to the atmosphere. Therefore, the injected solution should not be anoxic anymore and contain slightly less calcium due to its likely precipitation as calcite by reaction with the atmospheric CO_2. We chose to assume that the input is at equilibrium with respect to atmospheric oxygen in order to minimize the reduction of Tc in the system, and particularly, to avoid any reduction in the injection pipes. The solution is therefore at equilibrium with respect to both hematite and calcite.

Element	Modelled initial solution (mM/l)	Experimental data (mM/l)
Ca	35.60	29.8 - 32.5
Na	89.0	79.9 – 80.97 (*)
CO_3	0.70	1.49 – 1.61
Cl	150.2	137.7 - 144.5
Fe	0.016	0.012 – 0.013

(*) Includes the concentrations of K and Mg.

Table 4-12: Initial pore water concentrations.

In order to simulate adsorption, we added a surface complexation model based upon a hypothetical surface site (=*Site*) and using a set of reaction constants adjusted to allow the competition between Ca and Tc:

$$=Site\text{-}OH + Ca^{2+} \leftrightarrow =Site\text{-}OCa^{+} + H^{+} \qquad (\log_{10} K_{eq} = 2)$$

$$=Site\text{-}OH + TcO^{2+} + H_2O \leftrightarrow =Site\text{-}OTcOOH + 2\,H^{+} \qquad (\log_{10} K_{eq} = 8)$$

Note that compared to the approach in the main body of this report, the surface complexation model corresponds to modified assumptions. Firstly, we consider here that the "retention capacity" is homogeneous in the whole network (i.e. all surface sites

"=*Site*" are equivalent), so we do not examine the effect of the various materials coating the fracture sides. In this way this model is simpler than the "main model". Secondly, we allow here a competition between Calcium and Technetium for the adsorption sites. In this way, this model adds a degree of complexity, by taking into account the interaction between species, not only by chemical exchange but also by competition for the adsorption sites. However, the Calcium here is close to the background concentration, and remains relatively constant throughout the simulation. This means that in our retention model for Technetium, the adsorption part will be essentially linear.

4.4.3.3. Modelling results

The simulation is based upon the pipes network and the boundary conditions described in chapter 3. We simulated a period of 90 days. In fact, after about 40 days, the simulated breakthrough reaches a plateau of about 8 10^{-22} Bq/kg, very far below the level of detection of any experimental set-up. The concentrations shown in Figure 4-14 to Figure 4-19 are taken at the end of the 90-days simulation.

Figure 4-14 (expressed in total concentrations) and Figure 4-15 (expressed in soluble concentrations) show that Tc is essentially located close to the injection well and that the concentrations in the other part of the domain are negligible. Comparing with Figure 4-16, which displays the concentrations of Tc(IV) only, indicates that Tc is predicted to be essentially under this reduced redox state (the injection pipes excepted). Figure 4-17 and Figure 4-18 show that Tc is fixed essentially through the precipitation of TcS_2 at the injection borehole vicinity, and to a lesser extent, adsorption along the flow path.

Figure 4-19 displays the Tc concentrations in Bq/kg. The simulated breakthrough curve is displayed on Figure 4-20. and suggests that even by monitoring the test for a much longer period, we would not detect a breakthrough of Tc. The very low concentration at the outlet reaches a constant value due to the precipitation of TcS_2, which is limiting the maximum concentration at the value of the solubility of the mineral. The concentration of Tc at the pumping well should therefore remain stable as long as the local conditions, such as redox potential, do not significantly change.

In conclusion, the modelling results indicate that adopting an assumption of linearity for Tc may be too simplistic. It must be emphasised that the simulations performed would need more constraints to be validated. A much longer monitoring period, for example, would help decide if the precipitation effect predicted here is realistic, by checking the absence (or presence) of a breakthrough over a longer time span. However, such measurements would have been difficult to interpret because of the changes in boundary conditions during the test. Moreover, the kinetics of some reactions, such as pyrite dissolution or TcS_2 precipitation, should be investigated.

A plausible cause for the absence of Tc other than the "matrix diffusion – linear retention" hypothesis used in the main part of this report has been simulated. Using realistic values (from the *EQ3/6* database) for the various thermodynamic constants, and taking into account, besides the tracer, the main minerals detected in the *Feature A* groundwater, we effectively predict undetectable arrival. Such results call for a much more detailed study of the geochemical interactions at the experimental time frame before extrapolating to the Performance Assessment time frame. However, this would need to be based upon complex laboratory and *in-situ* investigations. We simply do not have enough data to go much further in this direction in the framework of the Task 6 project.

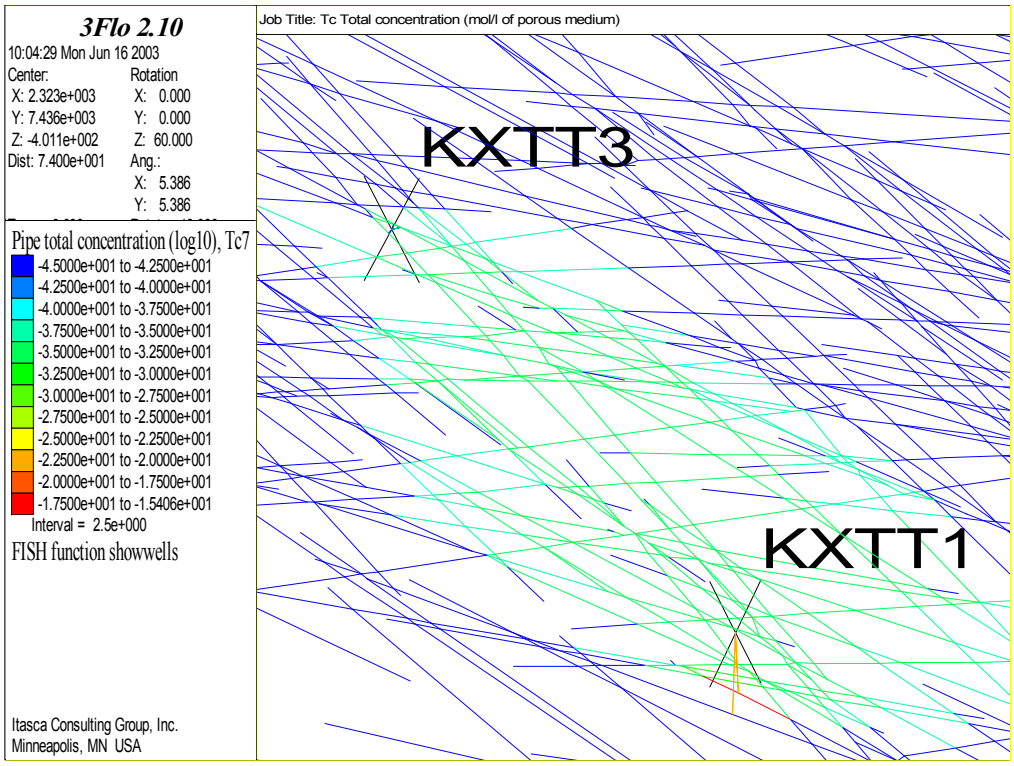

Figure 4-14 Tc total concentrations (M) - log10 scale. Lowest values (dark blue) can be lesser than the indicated range.

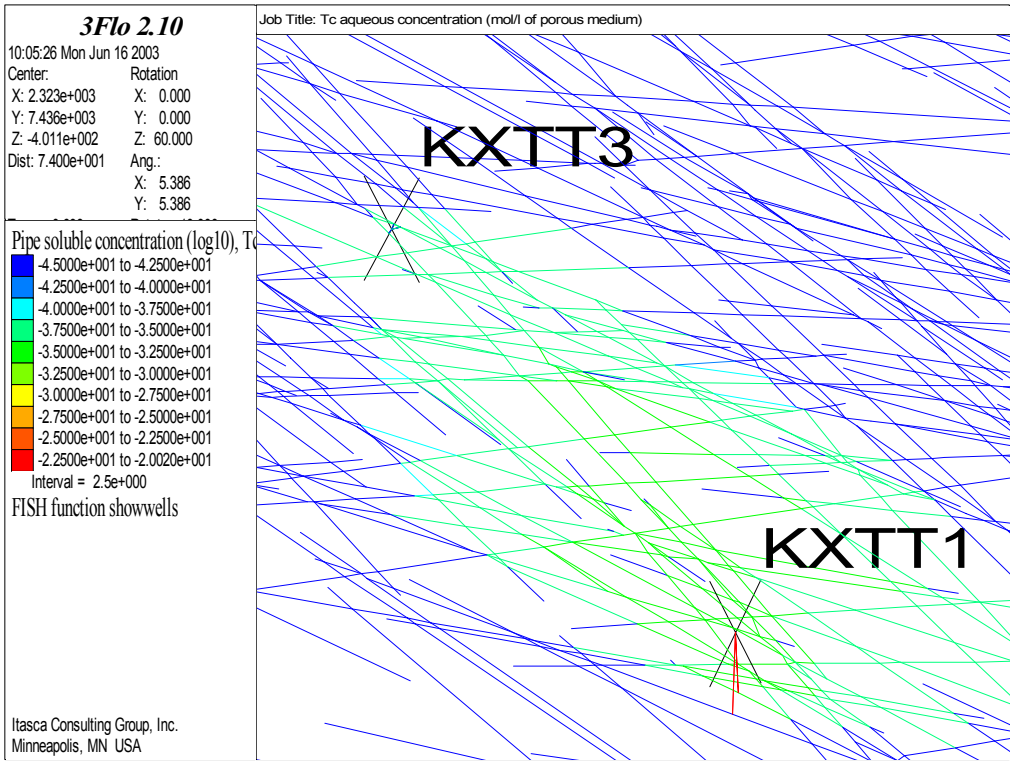

Figure 4-15 Tc total soluble concentrations (M) - log10 scale. Lowest values (dark blue) can be lesser than the indicated range.

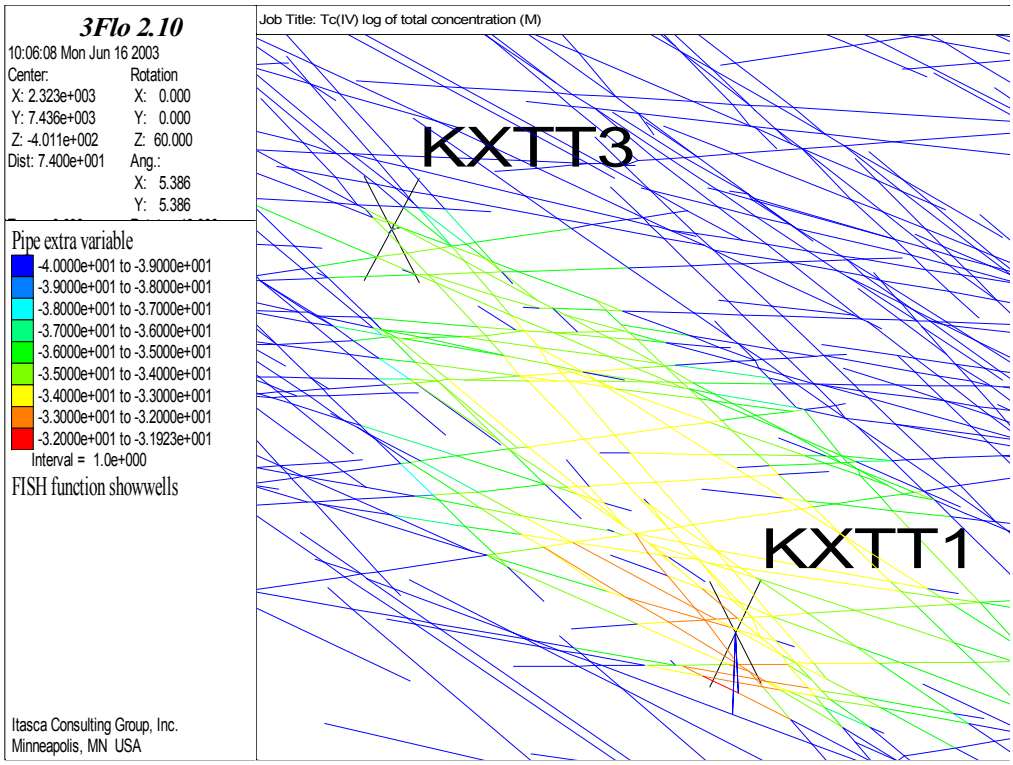

Figure 4-16 : Tc(IV) total concentrations (M) - log10 scale.

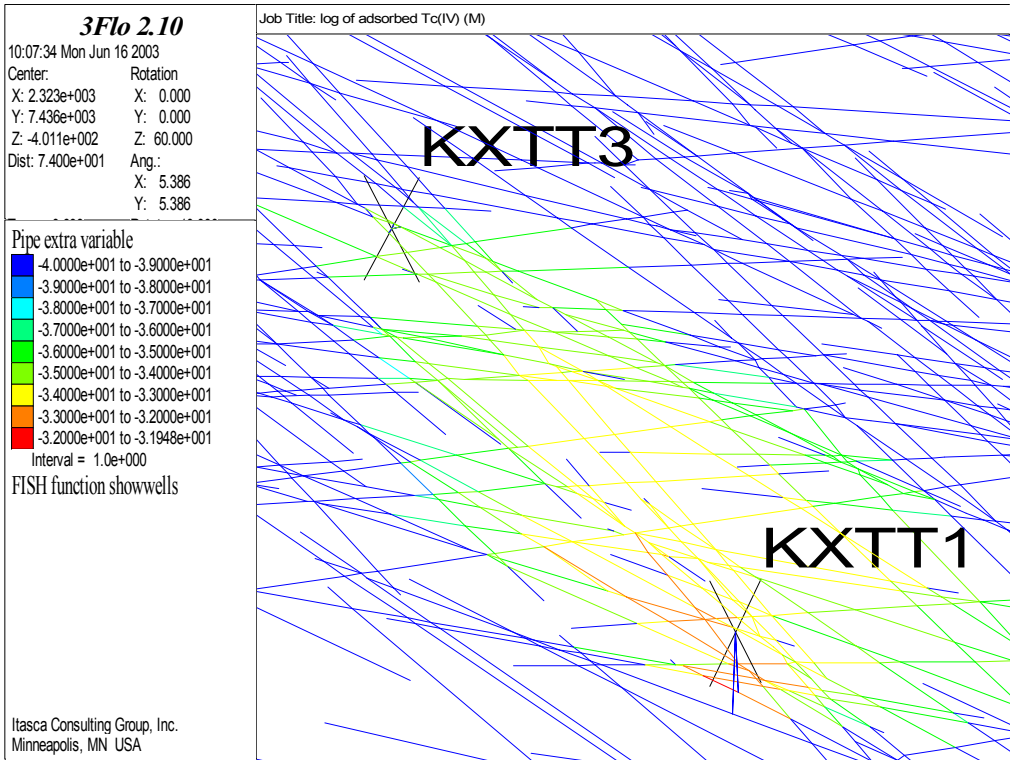

Figure 4-17 : Tc adsorbed concentration (M) - log10 scale.

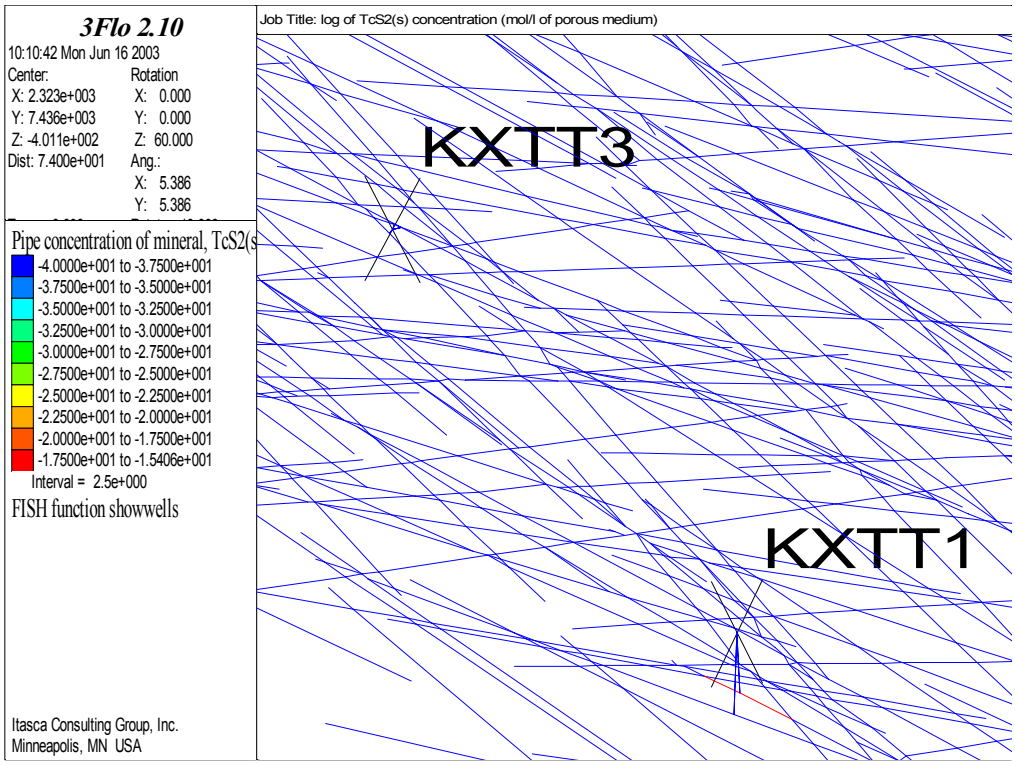

Figure 4-18 : TcS2(s) concentration (M) - log10 scale.

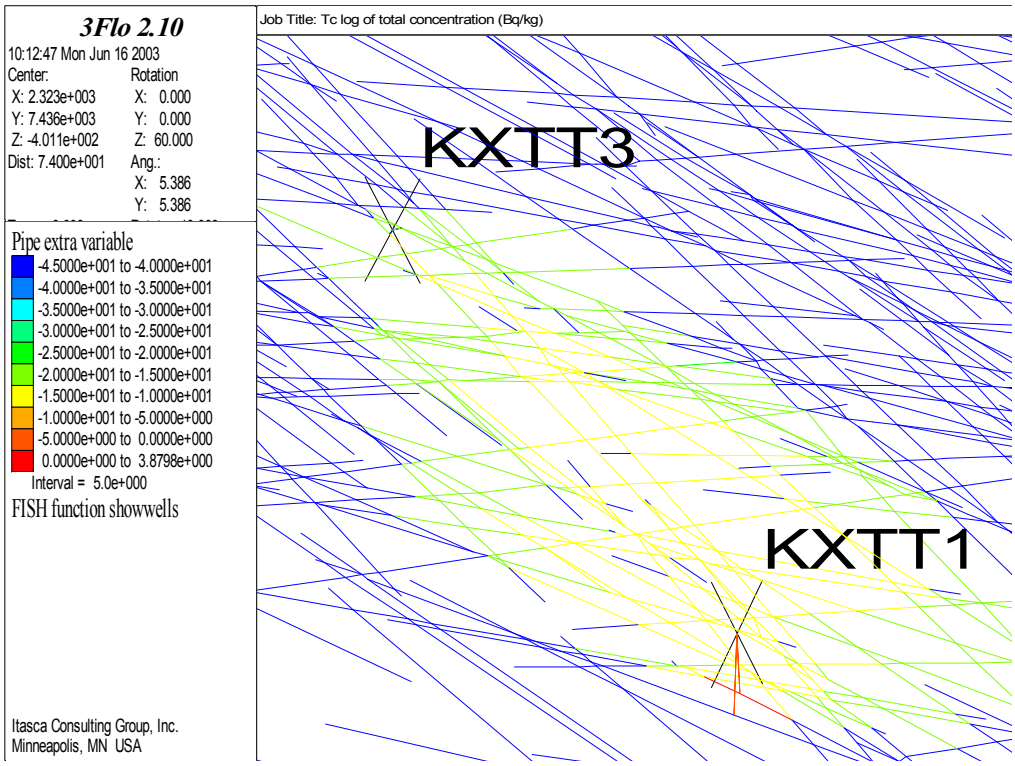

Figure 4-19 : Tc total concentrations (Bq/kg) - log10 scale.

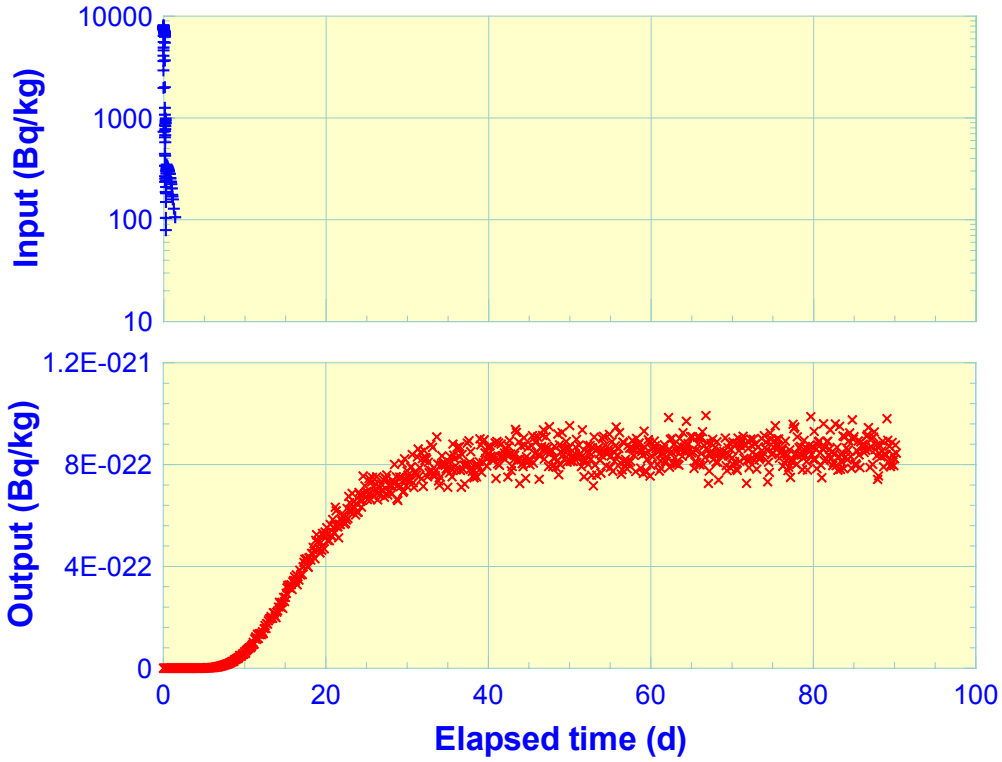

Figure 4-20 Tc input and computed breakthrough curve (Bq/kg).

5 Discussion

As stated in the introduction to this report, ITASCA Consultants had not participated in the previous ÄSPÖ HRL Task that simulated test STT-1b. Therefore, an initial aim of the work described here was to gain an understanding of Feature A through Task 6A before performing the long term simulations. In fact, this proved much more difficult than expected, with reactive tracer behaviour that was hard to reproduce within the conceptual framework of the so-called Advection-Dispersion-Diffusion, or ADD model.

- The properties needed to reproduce the Cobalt behaviour (longitudinal dispersivity coefficient) are not consistent with the properties needed for other tracers. Put in an other way, we have to consider that Cobalt samples a flow field that is somewhat different from the flow field sampled by Iodine and Strontium, although they where released at the same time in the same borehole. This problem may have many causes, all pertaining to the fact that the physics imbedded in our ADD model may overlook some phenomenon. Note that the problem may lay with the change in boundary conditions which occurred during the tracer test, and had more effect on the slower tracers.

- The model predicts a Technetium breakthrough although none has been recorded. We have shown that by taking explicitly speciation into account, we can reproduce the Technetium trapping. More experimental work would be needed to corroborate or refute the modified conceptual model.

So, even at the time scale of the tracer test, conceptual uncertainties remain large. Further proof of this can be found in the trial simulations using no diffusion to the matrix: it seems that an acceptable fit can be obtained with such a simplified model.

The consequences of such uncertainties for extrapolation in time are extreme: for example, the predicted time for 95% breakthrough of a Sr pulse, using the 6B2 boundary conditions, is divided by 1000 when using the “no diffusion” calibration, compared to the “main” calibration.

It is striking that, if we disregard the Cobalt and Technetium tracer tests, the overall results we obtain look consistent with each other. The relations between the results for the various boundary conditions we test and for the various tracers we simulate show no unexpected behaviour. For a given set of statistical properties in the fracture (the calibrated parameters), a sensitivity study shows variations from realisation to realisation within an order of magnitude. The variability is seemingly larger for the 6B ”focussed flow” boundary conditions than with the 6B2 ”generalized flow” boundary conditions. Compared to the large conceptual uncertainties, the variability in predicted response from realisation to realisation is quite small. All these results point towards an internal consistency of the numerical model, but do not necessarily warrant the actual relevance of the long term computations.

In other words, if we stay within one given conceptual framework and disregard inconsistent data, extrapolation to very large time scales is not the biggest cause for very large uncertainties. It is our lack of a proper understanding of the phenomena arising even at the experimental time scale which brings about such uncertainties.

Since the conceptual model is the most important source of uncertainty at P.A. scale, it is very important not to impose it on the various modelling groups. In this regard, a proposal for Task 6E that would consider one given numerical model (and therefore the whole conceptual framework it is built upon) as "truth" and check how a more or less complete knowledge of this "numerical truth" affects the uncertainty inherent in the P.A. simulations, seems somewhat dangerous.

We would therefore propose that within Task 6E, as much latitude as possible be given to the various groups, for them to experiment with differing conceptual models. Note that the coupled "transport – speciation" model we have tried for the Technetium simulations in Task 6A is only one example of an alternative route. In fact, it suffers a major drawback for P.A. studies, in that 1) relevant data are not sufficiently available, and 2) computing times are likely to become unmanageable when simulating P.A. timescales.

6 References

ANDERSSON P., JOHANSSON H., NORDQVIST R., SKARNEMARK G., SKÅLBERG M., and WASS E., 1998: True 1st stage tracer test programme –Tracer tests with sorbing tracers, STT-1. *SKB Technical report n°TR-97, 32 p + appendix*.

BENABDERRAHMANE H., DERSHOWITZ W, SELROOS J.O., UCHIDA M., AND WINBERG A., November 2000: Task 6: Performance Assessment Modeling Using Site Characterization Data (PASC). *Proposal to the Äspö Task Force on Numerical Modeling.*

BILLAUX D., and PARIS B., 2001: *3FLO* Version 2.0 – Calculs d'écoulements et de transport tridimensionnels. Volume 3 – Bases théoriques. *Internal report ITASCA Consultants, 98 p*.

ELERT M., and SELROOS J. 0., 2001: Task 6B2 – Modeling task specification - Version 1.0.

ELERT M., and SVENSSON H., 2001: Evaluation of modeling of the True-1 radially converging tests with sorbing tracers – The Äspö Task Force on modeling of groundwater flow and transport of solutes – Tasks 4E and 4F. *Draft report, 76 p*.

GRISAK G.E. & PICKENS J.F., 1981 – Solute transport through fractured media 1. The effect of matrix diffusion. – *Water Resource Research, 16 (4), 719-730*

NERETNIEKS I., 1980 – Diffusion in the rock matrix: an important factor in radionuclide retardation. . – *Journal of Geophysical Research, 85 (88), 4379-4397*

SELROOS J. 0., and ELERT M., 2001: Task 6A & 6B – Modeling task specification - Version 1.0. *25 p*.

VAN DER LEE J., 1991 – Radionuclide migration in the geosphere: modeling transport of colloids. – *Progress Report 91, ENSMP-CIG, Fontainebleau.*

WINBERG A., ANDERSSON P., HERMANSON J., BYEGÅRD J., CVETKOVIC V., and BIRGERSSON L., 2000: Äspö Hard Rock Laboratory – Final report of the first stage of the Tracer Retention Understanding Experiments. *SKB Technical report n°TR-00-07, 248 p*.

WOLERY T.J. (1992) : EQ3NR, A Computer Program for Geochemical Aqueous Speciation-Solubility Calculations: Theoretical Manual, User's Guide, and Related Documentation (Version 7.0). *LLNL, pp. 262*.

7 Appendix: validation of the procedure for diffusion to the matrix.

This appendix describes a validation test for the matrix diffusion procedure in 3FLO. A unit concentration of tracer is injected, starting at time t=0 in a 1-D channel. The velocity field is uniform and constant in time. The tracer is allowed to diffuse from the channel to a porous matrix, with an infinite thickness, and where advection velocity is 0. In the porous matrix, the tracer migrates normal to the channel, by diffusion only.

7.1.1 Analytical solution

An analytical solution to this problem is given by van der Lee (1991), using work by Neretnieks (1980) and by Grisak & Pickens (1981). Concentration *C* in a point of the channel is given by:

$$C = C_0 * erfc\left[\frac{x\sqrt{D_e}}{2bV\sqrt{t-\frac{x}{V}}}\right] \text{ if } t \geq \frac{x}{V},$$

$$C = 0 \text{ if } t \leq \frac{x}{V}$$

where:

C_0 : injected concentration,

x : distance from source along channel,

t : time,

2b : fracture thickness,

V : advection velocity in channel,

D_e : effective diffusivity in the porous matrix.

7.1.2 Numerical simulations

We use a channel with unit section and unit conductivity. Therefore, by applying a hydraulic gradient equal to 10^{-7}, we obtain an advection velocity of 10^{-7} m/s. We inject a Dirac (unit mass of tracer) at location *x=0* in a channel placed along the X axis. We observe the variations of concentration at location *x = 10 m*. By a simple time integration (sum of all masses passing at observation location), we obtain the variations of concentration due to a constant injection.

The channel thickness is 0.002 m. We vary the effective diffusivity D_e between $5\ 10^{-17}$ m^2s^{-1} and $5\ 10^{-13}$ m^2s^{-1}. Matrix thickness in the model is set to 200 m, equivalent to infinity.

Figure 7-1 to Figure 7-5 show the results we obtain using a 5000 particles injection. Arrival time as well as tail of the distributions are well reproduced, thus validating the procedure used by 3FLO for matrix diffusion simulations, both for "low diffusion" cases (Figure 7-1), and for highly diffusive cases (Figure 7-5).

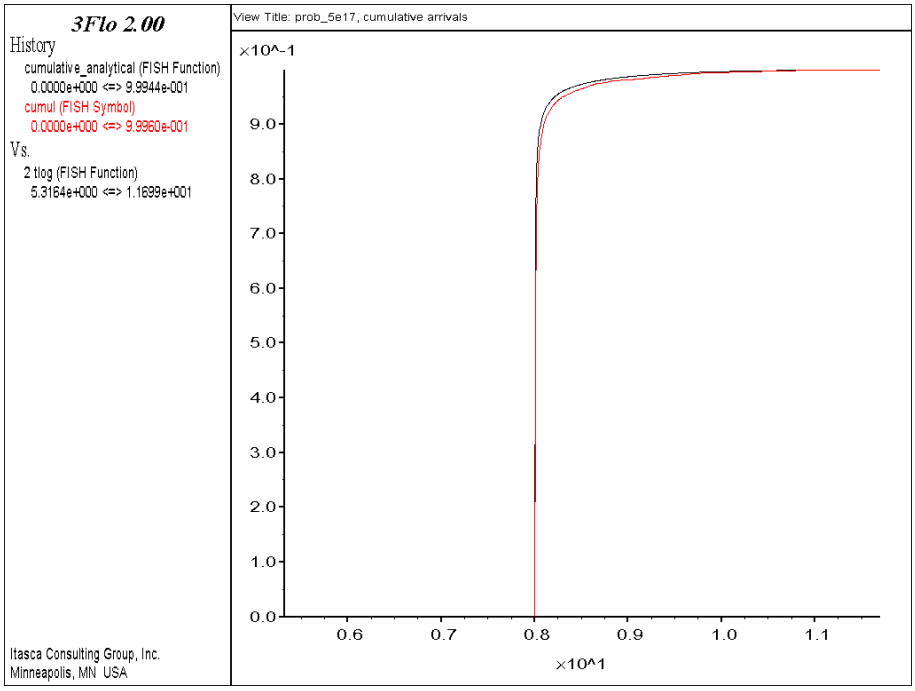

Figure 7-1 : Variations of concentration at location x=10 m with the decimal log of time. D_e=5 10^{-17} m^2s^{-1}. black : analytical – red: 3FLO.

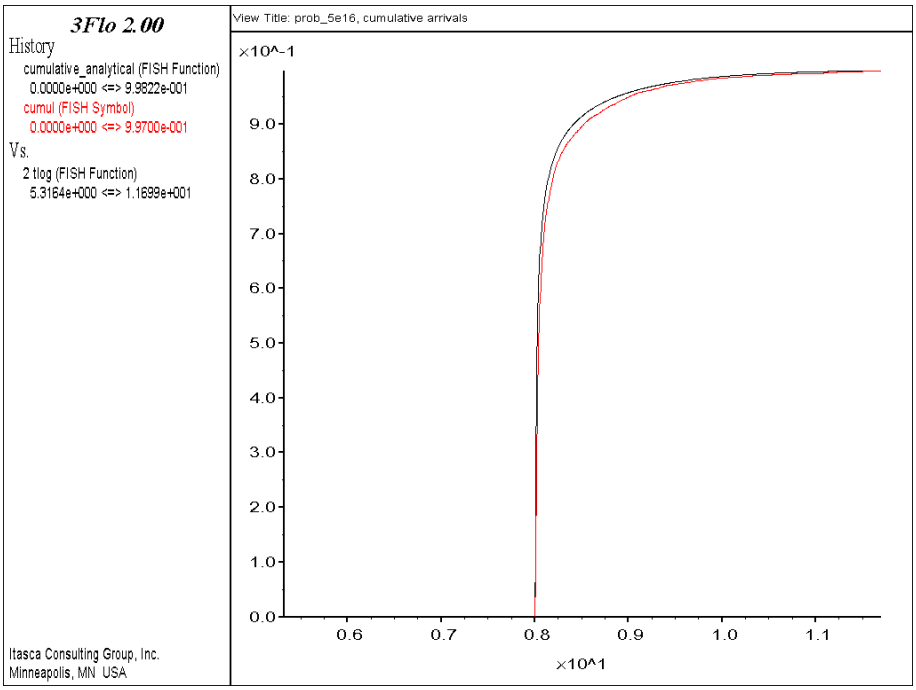

Figure 7-2 : Variations of concentration at location x=10 m with the decimal log of time. D_e=5 10^{-16} m^2s^{-1}. black : analytical – red: 3FLO.

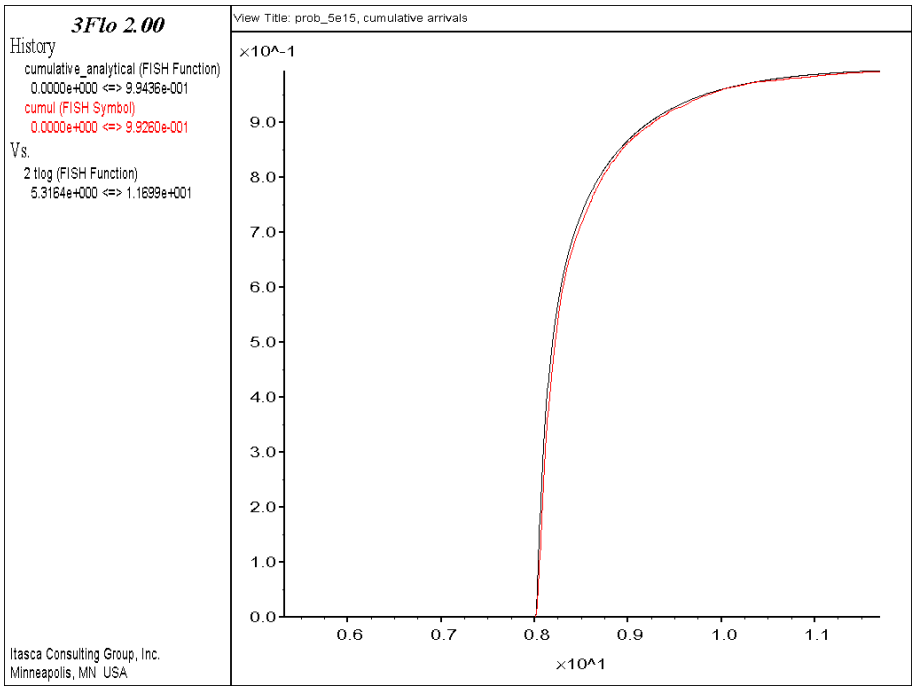

Figure 7-3 : Variations of concentration at location x=10 m with the decimal log of time. D_e=5 10^{-15} m^2s^{-1}. black : analytical – red: 3FLO.

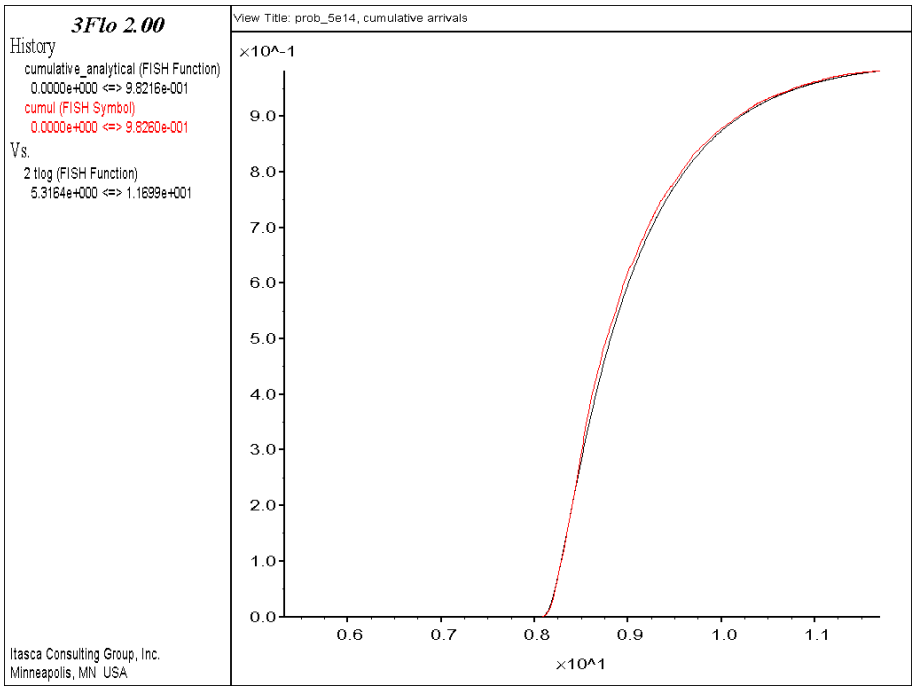

Figure 7-4 : Variations of concentration at location x=10 m with the decimal log of time. D_e=5 10^{-14} m^2s^{-1}. black : analytical – red: 3FLO.

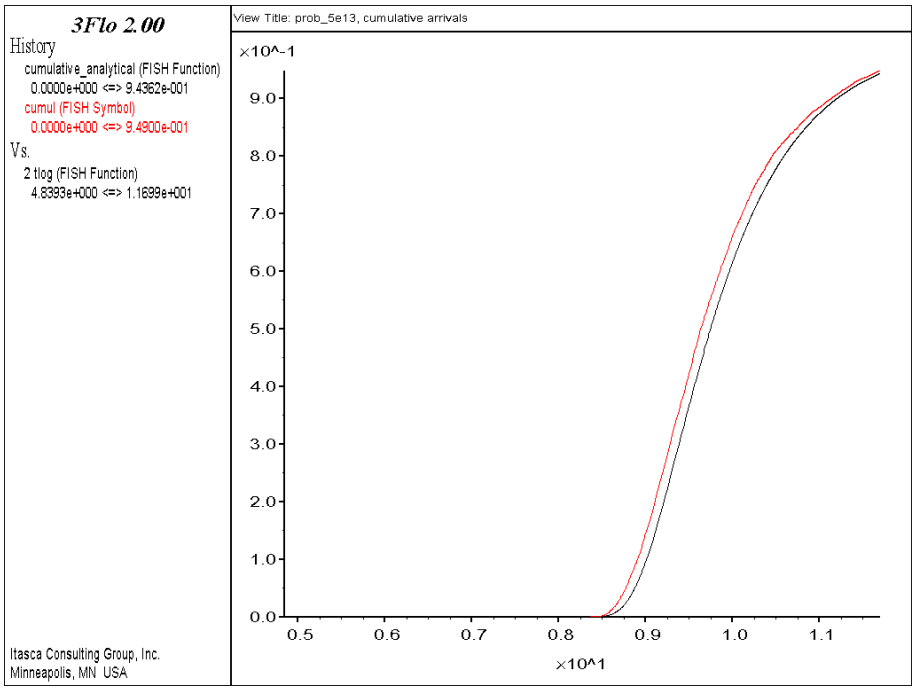

Figure 7-5 : Variations of concentration at location x=10 m with the decimal log of time. D_e=5 10^{-13} m^2s^{-1}. black : analytical – red: 3FLO.